Draft version December 23, 2016
Typeset using LaTeX **twocolumn** style in AASTeX61

arXiv:1612.07696v1 [astro-ph.GA] 22 Dec 2016

H I, CO, AND DUST IN THE PERSEUS CLOUD

Ryuji Okamoto,[1] Hiroaki Yamamoto,[1] Kengo Tachihara,[1] Takahiro Hayakawa,[1] Katsuhiro Hayashi,[1] and Yasuo Fukui[1]

[1] *Department of Physics, Nagoya University, Chikusa-ku, Nagoya 464-8602, Japan*

(Received; Revised; Accepted)

Submitted to ApJ

ABSTRACT

Comparison analyses between the gas emission data (H I 21 cm line and CO 2.6 mm line) and the *Planck*/*IRAS* dust emission data (optical depth at 353 GHz τ_{353} and dust temperature $T_{\rm d}$) allow us to estimate the amount and distribution of the hydrogen gas more accurately, and our previous studies revealed the existence of a large amount of optically-thick H I gas in the solar neighborhood. Referring to this, we discuss the neutral hydrogen gas around the Perseus cloud in the present paper. By using the J-band extinction data, we found that τ_{353} increases as a function of the 1.3-th power of column number density of the total hydrogen ($N_{\rm H}$), and this implies dust evolution in high density regions. This calibrated τ_{353}–$N_{\rm H}$ relationship shows that the amount of the H I gas can be underestimated to be ∼60% if the optically-thin H I method is used. Based on this relationship, we calculated optical depth of the 21 cm line ($\tau_{\rm H\,I}$), and found that $\langle\tau_{\rm H\,I}\rangle \sim 1.1$ around the molecular cloud. The effect of $\tau_{\rm H\,I}$ is still significant even if we take into account the dust evolution. We also estimated a spatial distribution of the CO-to-H_2 conversion factor ($X_{\rm CO}$), and we obtained $\langle X_{\rm CO}\rangle \sim 9.5 \times 10^{19}\,{\rm cm^{-2}\,K^{-1}\,km^{-1}\,s}$. Although these results are inconsistent with some previous studies, these discrepancies can be well explained by the difference of the data and analyses methods.

Keywords: ISM: atoms — ISM: molecules — ISM: individual objects (Perseus cloud)

Corresponding author: Ryuji Okamoto
okamoto@a.phys.nagoya-u.ac.jp

1. INTRODUCTION

The neutral atomic hydrogen (H I) 21 cm emission was discovered in the Galaxy in 1951, and has been used in order to investigate the structure of the Galaxy. It was revealed that the Galaxy has a spiral structure and is rotating at a nearly uniform velocity of $\sim$200 km s^{-1} except for within $\sim$2 pc from its center (e.g., Sofue 2013). The emission also brought advances in our understanding of the interstellar medium (ISM) and external galaxies. The role of hydrogen as the raw material of stars also attracted attention. In 1970's, the interstellar carbon monoxide (CO) emission at 2.6 mm was discovered and has been used as a tracer of molecular hydrogen (H_2) clouds, and a picture of the phase transition from H I to H_2 which triggers the star formation emerged. The molecular emission lines in the H_2 gas is efficient in cooling the gas which leads to release of the cloud internal energy and subsequent gravitational collapse.

Hydrogen (either atomic or molecular) accounts for the majority of the mass of the ISM; in the Galaxy, helium, which is abundant next to hydrogen, and heavier atoms account for $\sim$25% and $<$1% in mass, respectively. The volume number densities of the H I gas and the H_2 gas are estimated to be $\sim$1 cm^{-3} and $\sim$1000 cm^{-3}, respectively, on average. The physical states of the neutral gas at the intermediate density around 100 cm^{-3} are not understood into detail. In order to elucidate the evolution of the galaxies, it is an important task to better understand the behavior of the hydrogen gas including the transition from H I to H_2 over a density range 1–1000 cm^{-3}.

Planck is an astronomical satellite which aimed at observing the cosmic microwave background (CMB), and it observed the all sky at millimeter/sub-millimeter wavelengths (e.g., *Planck* Collaboration et al. 2011a). The data obtained by *Planck* necessarily include the emission from the ISM of the Galaxy as the foreground component of the CMB. By using the *Planck* data, physical parameters of the interstellar dust such as the optical depth at 353 GHz (τ_{353}), the dust temperature ($T_{\rm d}$), etc. are obtained, and they are available in the archival form (*Planck* Collaboration et al. 2014). These dust parameter data have relative uncertainties of $\lesssim$10%, and hence, we can expect that they accurately reflect the properties and states of the ISM at an angular resolution of 5 arcmin. In particular, τ_{353} is much less than 1 for all over the sky, even toward the Galactic plane, and therefore the data offer a reliable tracer of the column density of the total hydrogen atom ($N_{\rm H}$), if the dust-to-gas ratio (DGR) is a constant.

Fukui et al. (2014, 2015) compared the *Planck* dust data and the gas emission data such as H I and CO for the solar neighborhood. The H I 21 cm emission is generally assumed to be optically thin as written in text books. If the dust properties are uniform and DGR is a constant, it is expected that the velocity-integrated intensity of the 21 cm spectrum ($W_{\rm H\,I}$) is proportional to τ_{353} for the data points where the CO emission is not detected. Fukui et al. (2014, 2015) however found that the correlation between them is not so good. By introducing $T_{\rm d}$ into the τ_{353}–$W_{\rm H\,I}$ correlation plot, these authors discovered that the poor correlation in the τ_{353}–$W_{\rm H\,I}$ plot is mainly due to the data points where the density is high and $T_{\rm d}$ is low. Therefore, these authors concluded that there exists a large amount of optically thick H I gas in the local ISM whose typical optical depth is $\sim$1, and the amount of the H I gas is underestimated by $\sim$50% if a correction for the opacity effect is not applied. In Fukui et al. (2014, 2015), these analyses were made for the high Galactic latitude at $|b| > 15^\circ$ where the gas density is low. An open issue discussed in Fukui et al. (2014, 2015) is if τ_{353} obeys a simple linear relationship with the $N_{\rm H}$ or not. A study in the Orion A molecular cloud (Roy et al. 2013) indicates that the dust optical depth is proportional to the 1.28-th power of $N_{\rm H}$ rather than a simple linear relation. If correct, this non-linearity may be ascribed to the dust evolution at high column density. This suggests a possibility to apply a minor modification of the method of Fukui et al. (2014, 2015) in order to improve the accuracy in $N_{\rm H}$.

The Perseus cloud is one of the well-known molecular clouds in the solar neighborhood ($d \sim 300$ pc) located at $(\ell, b) \sim (160^\circ, -20^\circ)$ (e.g., Bally et al. 2008). This region is a part of the Gould's belt and the cloud includes some star forming regions (SFRs), IC 348 and NGC 1333, for example. There are a few previous studies on the interstellar hydrogen gas in the Perseus region such as Lee et al. (2012, 2014) and Stanimirović et al. (2014). Lee et al. (2012, 2014) estimated a spatial distribution of the $X_{\rm CO}$ factor, which is a conversion factor between the velocity-integrated intensity of ^{12}CO(J=1–0) line ($W_{\rm CO}$) and the column number density of the H_2 gas ($N_{\rm H_2}$). They used the *IRAS* 60, 100 μm data, and concluded that the average value of $X_{\rm CO}$ is $\sim 0.3 \times 10^{20}$ cm^{-2} K^{-1} km^{-1} s. This average value is significantly smaller than the typical value for the Galaxy, (1–2) $\times 10^{20}$ cm^{-2} K^{-1} km^{-1} s (e.g., Bolatto et al. 2013). In Stanimirović et al. (2014), the measurements of the optical depth of the H I gas ($\tau_{\rm H\,I}$) around the Perseus cloud were made. They observed the H I 21 cm absorption spectra toward 26 extra-Galactic radio continuum sources, and analyzed the data by using the method described in Heiles & Troland (2003). They concluded that optically-thick H I gas was detected only

toward ∼15% of the lines of sight, which disagrees with the results of Fukui et al. (2014, 2015), and cast doubt on the "optically-thick H I gas".

With these results in mind, the aims of the present study are as follows:

- To investigate whether the arguments by Fukui et al. (2014, 2015) still hold or not in the region where the density is relatively high and there exist the SFRs, and to explore if the τ_{353}–$N_{\rm H}$ relationship requires the non-linear relationship, suggesting dust evolution.

- To understand the cause for the difference between the previous results by Fukui et al. (2014, 2015), and Lee et al. (2012, 2014), Stanimirović et al. (2014) on $X_{\rm CO}$ and $\tau_{\rm H\,I}$, and to test the validity of usage of τ_{353} in order to estimate the amount of the hydrogen gas.

The present paper is organized as follows. Section 2 introduces the data set we used in the present study, and Section 3 describes the analyses methods and the results. We present the discussions in Section 4. Finally Section 5 summarizes the paper.

2. OBSERVATIONAL DATA SET

In the present paper, we used following gas and dust maps in order to investigate relationships between them. These data ware spatially smoothed to an effective HPBW (half power beam width) of 8.4 arcmin, which corresponds to that of the CfA CO data, except for the 21 cm radio continuum map (35 arcmin). Then, they were converted to a 3.0 arcmin grid spacing in Right Ascension and Declination.

2.1. *H I data*

Data sets of the GALFA H I survey (Data Release 1) (Peek et al. 2011) are used in the present study. This survey was done with the Arecibo Observatory 305 m telescope, and its HPBW is ∼4 arcmin. Note that we have linearly refitted the baseline of each spectrum using the velocity ranges of mainly $V_{\rm LSR} \leq -161\,{\rm km\,s^{-1}}$ and $V_{\rm LSR} \geq +112\,{\rm km\,s^{-1}}$ in order to correct the baseline offsets in this version of the raw GALFA data. Then, the data were spatially smoothed to be a 8.4 arcmin effective beam size, and RMS fluctuations of the smoothed data are ∼0.06 K at a $0.18\,{\rm km\,s^{-1}}$ velocity resolution.

2.2. *CO data*

We used the ^{12}CO(J=1–0) data cube by Dame et al. (2001) as a tracer of H_2 gas. The HPBW is 8.4 arcmin, and the RMS noise fluctuations are ∼0.25 K at a $0.65\,{\rm km\,s^{-1}}$ velocity resolution (Dame et al. 2001). We downloaded this data cube from the web site of Harvard-Smithsonian Center for Astrophysics (CfA)[1].

2.3. *Planck and IRAS dust emission data*

Archival data sets of dust optical depth at 353 GHz (τ_{353}) and dust temperature ($T_{\rm d}$) obtained by *Planck* and *IRAS* satellites are used. They were obtained by fitting intensities at 353 GHz, 545 GHz, and 857 GHz observed with *Planck* and at 100 μm of IRIS (Improved Reprocessing of the *IRAS* Survey) with modified-blackbody functions (for details, see *Planck* Collaboration et al. 2011b). In the present study we utilized version R1.20 of the *Planck* dust maps[2] and IRIS 60 μm and 100 μm maps[3] (Miville-Deschênes & Lagache 2005). We downloaded all-sky FITS data sets with a HEALPix[4] format (Górski et al. 2005).

2.4. *J-band extinction data*

An all-sky distribution of J-band extinction (A_J) was derived in Juvela & Montillaud (2016). They used "NICER" and "NICEST" methods in order to calculate the A_J map based on the 2MASS (two micron all-sky survey) J, H, and K-band extinction data. We downloaded an all-sky FITS data[5] with a HEALPix format. The angular resolution of the raw map is 3 arcmin.

2.5. *Hα data*

For the purpose of identifying regions where ultraviolet (UV) emission locally affect the dust properties by heating up or destroying them, we used Hα emission data. The Hα map was obtained by Finkbeiner (2003) and it has an angular resolution of 6 arcmin.

2.6. *21 cm radio continuum data*

21 cm continuum brightness temperature map is used in order to obtain the background emission. This map was derived by Reich & Reich (1986) and includes the 2.7 K cosmic background radiation. Although it has a lower spatial resolution (∼35 arcmin) than the other maps, we use this map as it is in the present study.

3. ANALYSES & RESULTS

3.1. *Spatial Distributions*

Figure 1 shows spatial distributions of data sets used in the present study.

[1] https://www.cfa.harvard.edu
[2] http://irsa.ipac.caltech.edu
[3] https://lambda.gsfc.nasa.gov
[4] http://healpix.sourceforge.net
[5] http://www.interstellarmedium.org

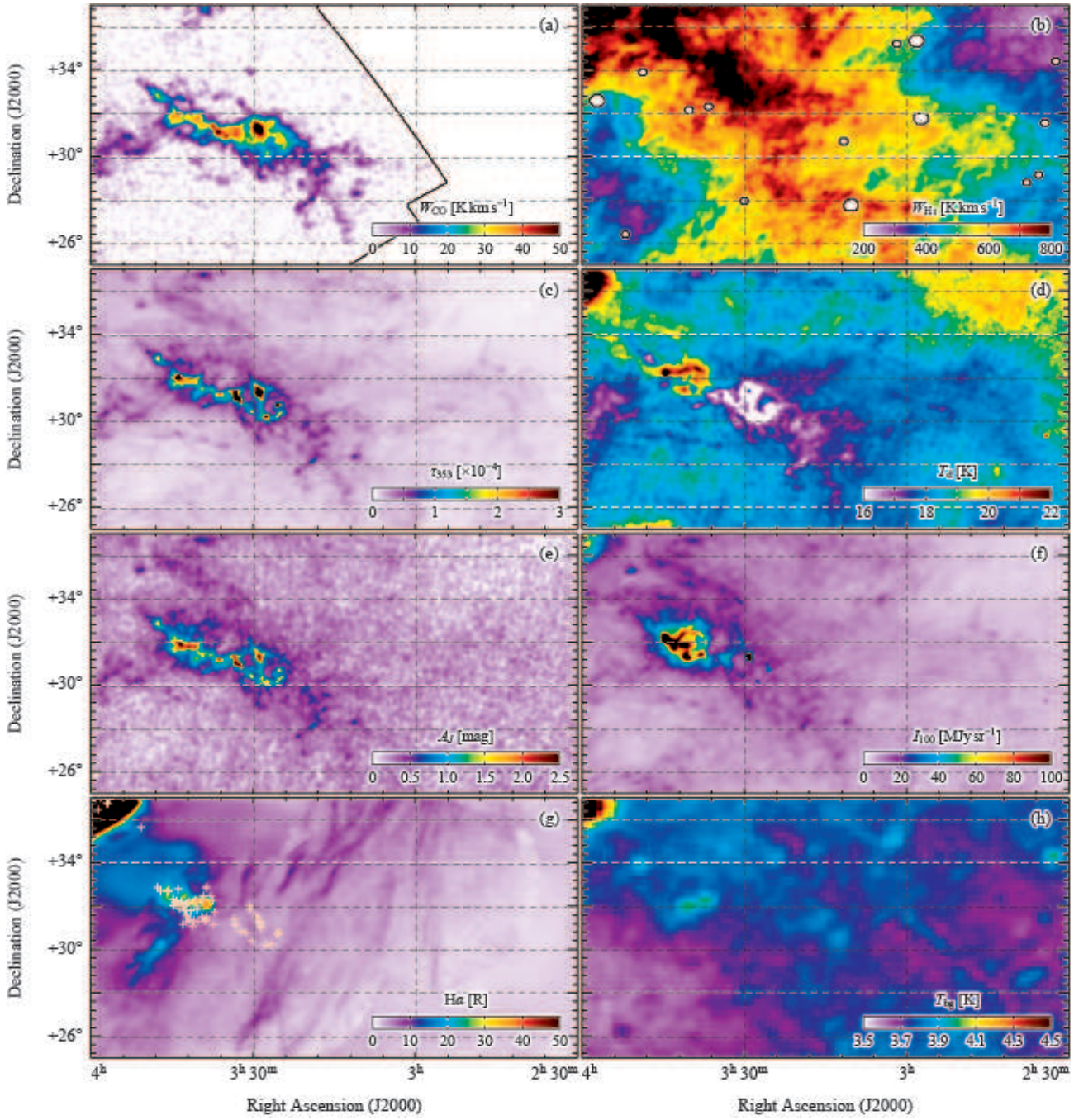

Figure 1. (a) A Velocity-integrated intensity map of ^{12}CO(J=1−0) line (Dame et al. 2001). The integrated velocity range is from $-4.9\,\mathrm{km\,s^{-1}}$ to $+12.0\,\mathrm{km\,s^{-1}}$. (b) A Velocity-integrated intensity map of H I 21 cm line (Peek et al. 2011). The integrated velocity range is from $-188.4\,\mathrm{km\,s^{-1}}$ to $+188.4\,\mathrm{km\,s^{-1}}$. See Figure 2 for the details of the masks. (c) and (d) Spatial distributions of optical depth at 353 GHz and cold dust temperature obtained by the *Planck*/*IRAS* satellites (*Planck* Collaboration et al. 2011b). (e) A map of J-band extinction derived by 2MASS data and "NICEST" analyses (Juvela & Montillaud 2016). (f) An intensity map at 100 μm obtained by *IRAS* satellite (Miville-Deschênes & Lagache 2005). (g) An Hα intensity map derived by Finkbeiner (2003). Red crosses indicate positions of YSO candidates (Tóth et al. 2014). (h) A spatial distribution of the 21 cm background radio continuum (Reich & Reich 1986). This map includes the 2.7 K cosmic background radiation, etc. Effective beam sizes are 8.4 arcmin for the panels (a)–(g), and 35 arcmin for the panel (h).

Table 1. List of symbols used in the present paper

Symbol	Unit	Description	Note
$W_{\rm H\,I}$	[K km s^{-1}]	H I 21 cm line velocity-integrated intensity.	(a)
$N_{\rm H\,I}$	[cm^{-2}]	H I column number density.	
$N^{*}_{\rm H\,I}$	[cm^{-2}]	H I column number density (optically thin limit), $\equiv X_{\rm H\,I}\times W_{\rm H\,I}$.	
$T_{\rm H\,I}$	[K]	H I brightness temperature.	
$\Delta V_{\rm H\,I}$	[km s^{-1}]	H I velocity width, $\equiv W_{\rm H\,I}/T_{\rm H\,I}$(peak).	
$\tau_{\rm H\,I}$	$\cdots$	H I optical depth.	
$T_{\rm s}$	[K]	H I spin temperature.	
$X_{\rm H\,I}$	[cm^{-2} K^{-1} km^{-1} s]	Theoretical conversion factor, $=1.823\times10^{18}$ cm^{-2} K^{-1} km^{-1} s.	
$N_{\rm H_2}$	[cm^{-2}]	H_2 column number density.	
$N_{\rm H}$	[cm^{-2}]	Total hydrogen column number density, $=N_{\rm H\,I}+2\,N_{\rm H_2}$.	
$W_{\rm CO}$	[K km s^{-1}]	^{12}CO(J=1–0) line velocity-integrated intensity.	(b)
$X_{\rm CO}$	[cm^{-2} K^{-1} km^{-1} s]	Empirical CO-to-H_2 conversion factor, $\equiv N_{\rm H_2}/W_{\rm CO}$.	
τ_{353}	$\cdots$	Optical depth at 353 GHz derived by *Planck*/*IRAS* satellite.	
$T_{\rm d}$	[K]	Cold dust temperature derived by *Planck*/*IRAS* satellite.	
A_J	[mag]	J-band extinction derived by NICEST method.	(c)
$T_{\rm bg}$	[K]	Background brightness temperature at 21 cm.	(d)
$\tau_{353,\rm ref}$	$\cdots$	Reference value of τ_{353}, $=1.6\times10^{-6}$.	(e)
$N_{\rm H,ref}$	[cm^{-2}]	Reference value of $N_{\rm H}$, $=3.4\times10^{20}$ cm^{-2}.	(e)
α	$\cdots$	Power index in Equation (2).	

Note— (a) Peek et al. (2011). The integrated range is from -188.4 km s^{-1} to $+188.4$ km s^{-1}.
(b) Dame et al. (2001). The integrated range is from -4.9 km s^{-1} to $+12.0$ km s^{-1}.
(c) Juvela & Montillaud (2016)
(d) Reich (1982); Reich & Reich (1986)
(e) Appendix A

Figure 1(a) is the distribution of velocity-integrated intensity of ^{12}CO(J=1−0) line ($W_{\rm CO}$) obtained by Dame et al. (2001). The integrated velocity range is from $-4.9\,{\rm km\,s^{-1}}$ to $+12.0\,{\rm km\,s^{-1}}$. We use this map as a tracer of column number densities of molecular hydrogen ($N_{\rm H_2}$).

Figure 1(b) is a map of velocity-integrated intensity of H I 21 cm line ($W_{\rm HI}$). It was derived by GALFA-H I survey (Peek et al. 2011). The integrated velocity range is from $-188.4\,{\rm km\,s^{-1}}$ to $+188.4\,{\rm km\,s^{-1}}$. Because we found some strong spike noises in the spectra in our region, we masked 4 areas to exclude these bad spectra. See Figure 2 for details on the mask.

Figure 1(c) and (d) show distributions of the dust emission parameters obtained from the *Planck*/*IRAS* observations. A map of dust optical depth at 353 GHz (τ_{353}) is drawn in Figure 1(c). τ_{353} is obtained by using the data observed with the *Planck* satellite, which is aimed at accurately detecting the spatial distribution of the CMB. Therefore, it has high reliability with typical uncertainty of $\lesssim$10%. In addition, the value of τ_{353} is at most $\lesssim 10^{-3}$ even toward the Galactic plane, and hence we can expect that it perfectly reflects the distribution and amount of ISM. τ_{353} is considered as a high accuracy/precision tracer of column number density of total hydrogen atoms ($N_{\rm H}$) if DGR is uniform.

Figure 1(d) shows cold dust temperature ($T_{\rm d}$) obtained simultaneously with τ_{353}. We can see a trend that $T_{\rm d}$ becomes lower toward the molecular clouds detected by CO. It indicates that dust grains themselves shield the interstellar radiation field (ISRF) in the molecular clouds and grains are less heated in addition to radiative cooling (see also Figure 5). Note that $T_{\rm d}$ is high around local heating sources, such as the California Nebula (NGC 1499), the Pleiades (M45), and the "ring-like feature" described in Lee et al. (2012). The $T_{\rm d}$ image has a relatively low contrast compared to τ_{353}, in particular the range of $T_{\rm d}$ in this region is typically from 17 K to 22 K. This is because $T_{\rm d}$ is proportional to the one-sixth power of the total intensity radiated from thermal-equilibrium grains expressed as the modified-blackbody model. It reflects that the total radiation energy of the modified-blackbody is proportional to the fourth power of the temperature, and is in addition proportional to the emissivity spectral index ($\sim$2).

Figure 1(e) is an image of J-band extinction (A_J) derived by (Juvela & Montillaud 2016) using 2MASS data and "NICEST" method (Lombardi & Alves 2001). We use this map as an another tracer of $N_{\rm H}$.

A spatial distribution of IRIS 100 μm intensity (I_{100}) is drawn in Figure 1(f). This map is used for a comparison of the CO-to-H$_2$ conversion factor (see Section 4.1).

We show an intensity map of Hα emission in Figure 1(g), overlaid with locations of young stellar object (YSO) candidates. Hα emission indicates the presence of ionized hydrogen (H II) and thus indicates the presence of strong UV radiation. We use the data in order to identify the region where the dust may be destroyed by UV radiation. The red crosses are the location of YSO candidates catalogued by Tóth et al. (2014). From this catalogue we extracted the candidates under the condition that "probability of being a YSO candidate" is greater than 0.997. It is based on AKARI Far-Infrared Surveyor (FIS) Bright Source Catalogue.

Figure 1(h) shows a spatial distribution of brightness temperature of 21 cm continuum radiation. This map was derived by Reich & Reich (1986) and includes the 2.7 K cosmic background radiation, etc.

3.2. *Masking*

Masks applied in the present study are shown in Figure (2).

(a) This mask is used in order to mask the data points which molecular hydrogen can exist ($W_{\rm CO} > 3\,\sigma$).

(b) There exist strong spike noises (equivalent to $T_{\rm HI} \sim 30$ K) in some spectra of GALFA-H I DR1 data. This mask is used in order to exclude the data points within 8.4 arcmin (= 1 HPBW) from these bad spectra.

(c) In Stanimirović et al. (2014) absorption spectra due to the local H I gas are detected toward extra-Galactic radio continuum sources. Since there are 11 out of these sources in this region, this mask is used to exclude the data points within 8.4 arcmin (= 1 HPBW) from them.

(d) This mask excludes the data points within 1.5 deg from the center of the Pleiades ($\alpha_{\rm J2000}, \delta_{\rm J2000}$) $\sim$ ($3^{\rm h}\,47^{\rm m}, +24^\circ\,07^{\rm m}$) (SIMBAD Astronomical Database, Wenger et al. 2000) because dust grains are locally heated up.

(e) Lee et al. (2012) describes the "ring-like feature", which is formed by an H II region due to a B-type star named HD 278942 (Ridge et al. 2006). As well as Lee et al. (2012) this mask is used to exclude the data points within 56 arcmin from ($\alpha_{\rm J2000}, \delta_{\rm J2000}$) = ($3^{\rm h}\,39^{\rm m}\,30^{\rm s}, +32^\circ$).

(f) Dust grains can be locally heated up or destroyed in regions where Hα emission is strong. We use this mask for the purpose of excluding the data points where H$\alpha \geq 10$ R.

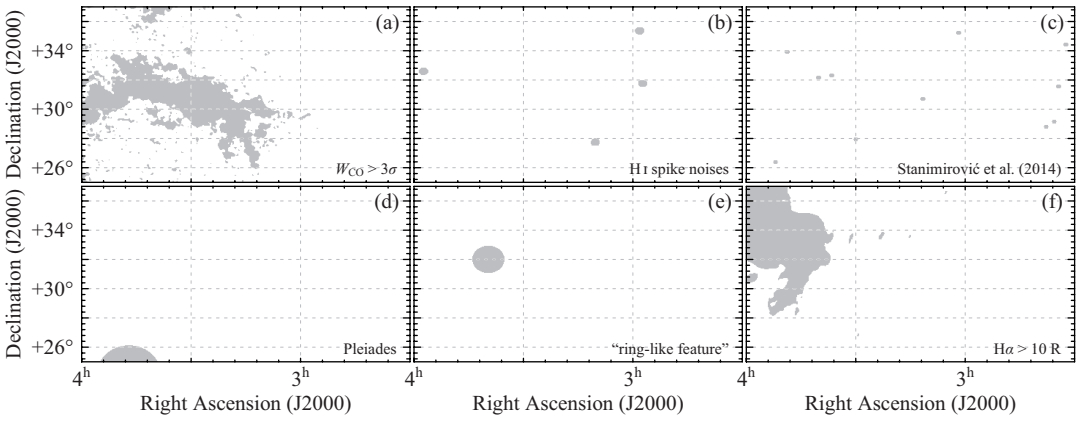

Figure 2. Mask maps used in the present study. We masked the data points (a) where $W_{\rm CO} \geq 3\,\sigma$, (b) where spike noises are detected in H I spectra, (c) within an effective HPBW (8.4 arcmin) of background radio point sources described in Stanimirović et al. (2014), (d) within 1.5 deg of Pleiades, (e) within 56 arcmin from $(\alpha_{\rm J2000}, \delta_{\rm J2000}) = (3^{\rm h}\,39^{\rm m}\,30^{\rm s}, +32^\circ)$ ("ring-like feature" described in Lee et al. 2012), and (f) where H$\alpha \geq 10$ R. (b) and (c) are applied to H I maps, (d), (e), and (f) are applied to dust maps.

Mask-(a) is applied to Figure 6, 7(c), 8, 9. Mask-(b), (c) are applied to the H I data, and mask-(d), (e), (f) to the dust data.

3.3. *Velocity Structure*

Figure 3(a) is a R.A.-velocity diagram of H I (image) and CO (contours, every 0.3 K from 0.3 K) in terms of Dec.-averaged intensities. Figure 3(b) shows the mean H I spectrum of this region. Although there is a intermediate-velocity component (intermediate-velocity cloud; IVC) at $V_{\rm LSR} \lesssim -30\,{\rm km\,s^{-1}}$, its contribution to the column density is only up to ∼6% of the total, we therefore use the data including all the velocity components.

3.4. *Hydrogen Abundance Estimation*

Figure (4) is a double logarithmic correlation plot between A_J and τ_{353}. A linear regression in double logarithmic scale using the data of $A_J \geq 0.5$ mag and $\tau_{353} \geq 3 \times 10^{-5}$ yields the following relationship,

$$\tau_{353} = (1.13 \times 10^{-4}) \times (A_J)^{1.25}. \quad (1)$$

Considering A_J as a linear tracer of $N_{\rm H}$ along each line of sight, Equation (1) indicates that dust emission cross section per hydrogen atom increases with the 1.25-th power of $N_{\rm H}$. A similar analysis was done in Roy et al. (2013) for the Orion A region, and they concluded that the power index is 1.28. Our result is consistent with it, and these results show dust evolution in high density regions. The grain size is typically up to ∼0.2 μm (Jones et al. 2013), which is much smaller than the J-band wavelength, ∼1.25 μm. In addition, the grain size can change by only ∼0.02 μm (Ysard et al. 2015). Roy et al. (2013) and Forbrich et al. (2015) also argue that in the high density regions it is mostly the sub-millimeter opacity that is changing, not the infrared extinction. Therefore, changes in the grain size have small effect on the J-band extinction, and we can regard A_J as a linear tracer of $N_{\rm H}$ if DGR is uniform. In the present study, therefore, we adopted 1.3 as the power index (α) from Equation (1).

In Fukui et al. (2014, 2015) we suggested an algorithm for estimating the amount of the hydrogen gas using τ_{353} as an accurate tracer of $N_{\rm H}$. In Fukui et al. (2014) we assumed the relationship $\tau_{353} \propto N_{\rm H}$. On the other hand, Fukui et al. (2015), considering the result of Roy et al. (2013), made discussion using the relationship of

$$\frac{\tau_{353}}{\tau_{353,{\rm ref}}} = \left(\frac{N_{\rm H}}{N_{\rm H,ref}}\right)^{\alpha}. \quad (2)$$

Here $\tau_{353,{\rm ref}}$ and $N_{\rm H,ref}$ are normalization constants which satisfy the relationship of $N_{\rm H,ref} = (1.15 \times 10^8) \times X_{\rm H\,I} \times \tau_{353,{\rm ref}}$ (Fukui et al. 2015). In the present study we use Equation (2) by substituting $\alpha = 1.3$, $\tau_{353,{\rm ref}} = 1.6 \times 10^{-6}$, and $N_{\rm H,ref} = 3.4 \times 10^{20}\,{\rm cm^{-2}}$;

$$\begin{aligned} N_{\rm H} &= \left(\frac{\tau_{353}}{\tau_{353,{\rm ref}}}\right)^{1/\alpha} N_{\rm H,ref} \quad (3) \\ &= (9.8 \times 10^{24}) \times (\tau_{353})^{1/1.3}. \end{aligned}$$

See Appendix A for the details of the determination of $\tau_{353,{\rm ref}}$ and $N_{\rm H,ref}$.

Conventionally, the following equation is used to calculate the column number density of H I gas from an observable value, $W_{\rm H\,I}$,

$$N^*_{\rm H\,I} \equiv X_{\rm H\,I} \times W_{\rm H\,I}. \quad (4)$$

Although widely used, this equation is obtained under the assumption that the H I gas is optically thin

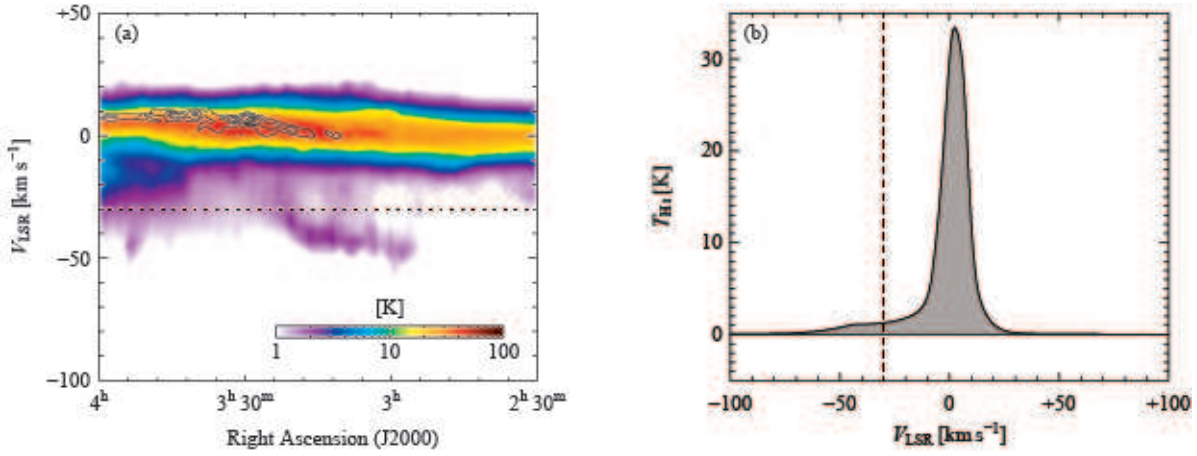

Figure 3. (a) A R.A.-velocity diagram of H I (image) and CO (contours) in terms of Dec.-averaged intensities. The contours are drawn every 0.3 K from 0.3 K. The average is calculated over the whole Dec. range shown in Figure (1). (b) An averaged H I spectrum calculated over the whole region shown in Figure (1) (b). The dashed lines indicate $V_{\rm LSR} = -30\,{\rm km\,s^{-1}}$.

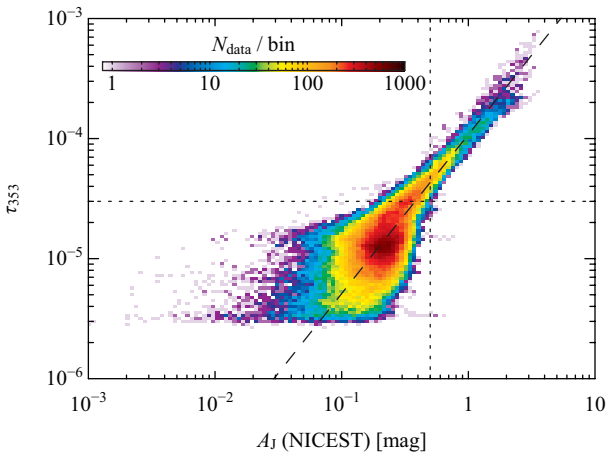

Figure 4. A double logarithmic scatter plot (density plot) between A_J and τ_{353}. Colors are correspond to numbers of the data points included in each bin. The solid line shows a relationship of $\tau_{353} = (1.13 \times 10^{-4}) \times (A_J)^{1.25}$, which is the result of a linear regression in double logarithmic scale using the data of $A_J \geq 0.5$ mag and $\tau_{353} \geq 3 \times 10^{-5}$. The dashed lines indicate $A_J = 0.5$ mag and $\tau_{353} = 3 \times 10^{-5}$.

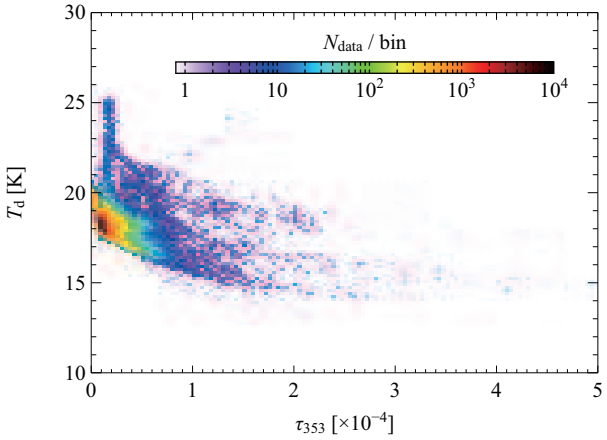

Figure 5. A scatter plot (density plot) between τ_{353} and $T_{\rm d}$. It clearly shows a negative relationship as with Fukui et al. (2014) for MBM 53, 54, 55 region.

($\tau_{\rm HI} \ll 1$). The symbol $N^*_{\rm HI}$ is the H I column number density in the optically-thin limit. Therefore, when Equation (4) is used, the H I column number density can be underestimated if optically-thick H I gas exists. Here we will show that H I optical depth has significant effects on the estimation of the H I amount in the Perseus region.

Figure 5 is a scatter plot between τ_{353} and $T_{\rm d}$ of the region analyzed. As well as the MBM 53, 54, 55 region (Fukui et al. 2014), it clearly shows an anti-correlation relationship between the two quantities. As described in Section 3.1, dust grains are heated by interstellar radiation field (ISRF). In the areas where τ_{353} is small, the amount of ISM is also small and therefore the ISRF efficiently heats up the dust grains. Conversely, in the areas where τ_{353} is large, the amount of ISM is also large and the ISRF is shielded by the grains themselves, and they are cooled by dust radiation. The anti-correlation in Figure 5 reflects these picture. In addition, in the latter case, the dust growth can increase τ_{353} in such high density areas.

Figure 6 is a correlation plot between τ_{353} and $W_{\rm HI}$ colored by $T_{\rm d}$ in windows of 0.5 K intervals. Note that we applied the mask-(a) (CO mask) and therefore, $N_{\rm H} = N_{\rm HI}$ for the data points plotted in Figure 6. Although the correlation is not so good as a whole, the distributions of the data points on the τ_{353}–$W_{\rm HI}$ plane are clearly different when separated according to $T_{\rm d}$. The scattering is small for the data points where $T_{\rm d}$ is high, and it becomes large with decreasing $T_{\rm d}$. In particular, the distribution of the high-$T_{\rm d}$ points (such as $T_{\rm d} > 19.5$ K) is elongated, and it seems to pass through

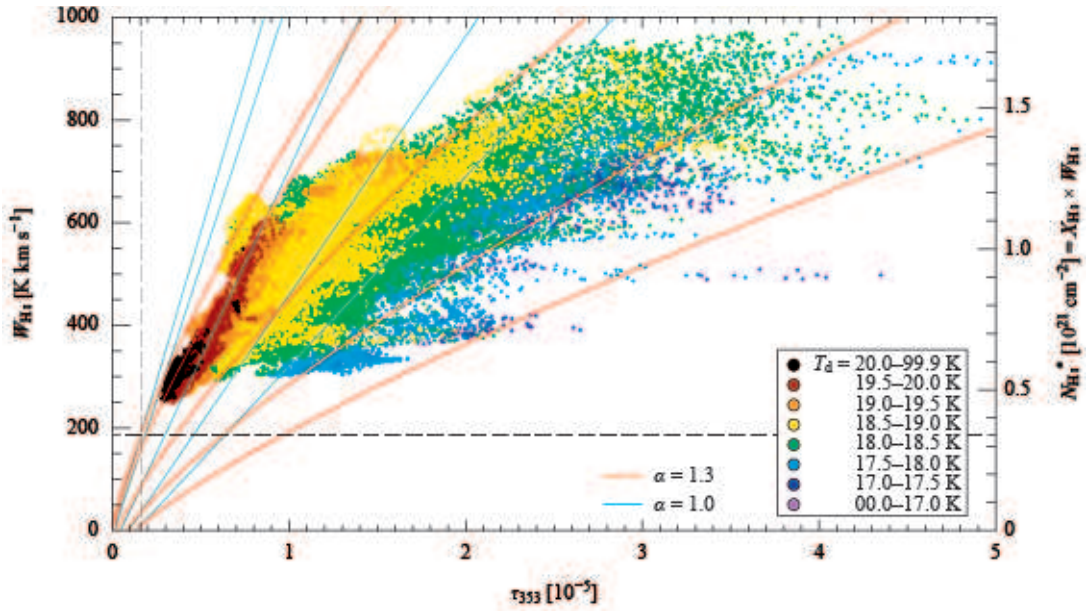

Figure 6. A scatter plot between τ_{353} and $W_{\rm H\,I}$ colored by $T_{\rm d}$ in 0.5 K windows. The right hand y-axis indicates the column number density of H I in the optically-thin limit ($N_{\rm H\,I}$). The curves are theoretical relationships between both variables (Equation (7)) for the case of $\tau_{\rm H\,I} = 0, 0.21, 1, 2, 3$ (from left to right). The light blue ones are for the case of $\alpha = 1.0$ and red ones for the case of $\alpha = 1.3$, respectively. We considered $T_{\rm bg} = 3.7$ K and $\Delta V_{\rm H\,I} = 13.7\,{\rm km\,s^{-1}}$ (mean values in this region) as constants. The dashed lines correspond to $\tau_{353,\rm ref} = 1.6 \times 10^{-6}$ and $N_{\rm H,ref} = 3.4 \times 10^{20}\,{\rm cm^{-2}}$ (Appendix A).

the origin when it is extrapolated. On the other hand, the distribution of the low-$T_{\rm d}$ points is broadened along the τ_{353} axis. As we described above, this indicates that for such low-$T_{\rm d}$ points the amount of the ISM is large, and hence $W_{\rm H\,I}$ is saturated against τ_{353} because of the effect of large optical depth, i.e., $\tau_{\rm H\,I} \gtrsim 0.3$. Therefore, for such data points the amount of H I cannot be calculated by using Equation (4). It can be said that the reason of the low spatial correlation between τ_{353} and $W_{\rm H\,I}$ (Figure 1(b), (c)) is the effect of $\tau_{\rm H\,I}$. This aspect of the $W_{\rm H\,I}$ saturation can be explained by using the radiation transfer equation as stated below.

The following Equations (5) and (6) are the radiation transfer equation of H I 21 cm line and the equation of H I optical depth, respectively, and both of them are derived theoretically (e.g., Draine 2011; Dickey & Lockman 1990).

$$W_{\rm H\,I} = (T_{\rm s} - T_{\rm bg})\,\Delta V_{\rm H\,I}\,\{1 - \exp(-\tau_{\rm H\,I})\} \quad (5)$$

$$\tau_{\rm H\,I} = \frac{N_{\rm H\,I}}{X_{\rm H\,I}}\,\frac{1}{T_{\rm s}}\,\frac{1}{\Delta V_{\rm H\,I}} \quad (6)$$

These equations are independent of each other, and are valid regardless of whether $\tau_{\rm H\,I}$ is negligible or not.We define $\Delta V_{\rm H\,I}$ as $W_{\rm H\,I}/T_{\rm H\,I}$(peak), and $\tau_{\rm H\,I}$ in Equations (5) and (6) are regarded as the average values over the velocity range $\Delta V_{\rm H\,I}$. From the two and Equation (3) we derive the following relationship;

$$W_{\rm H\,I} = \left\{ \left(\frac{\tau_{353}}{\tau_{353,\rm ref}} \right)^{1/\alpha} \frac{N_{\rm H,ref}}{X_{\rm H\,I}}\,\frac{1}{\tau_{\rm H\,I}}\,\frac{1}{\Delta V_{\rm H\,I}} - T_{\rm bg} \right\} \times \Delta V_{\rm H\,I}\,\{1 - \exp(-\tau_{\rm H\,I})\}. \quad (7)$$

The lines/curves in Figure 6 show this relationships in cases of $\alpha = 1.0, 1.3$ (light blue lines and red curves, respectively) when $\tau_{\rm H\,I} = 0, 0.21, 1, 2, 3$ are substituted (from left to right). We applied $\Delta V_{\rm H\,I} = 13.7\,{\rm km\,s^{-1}}$ and $T_{\rm bg} = 3.7$ K, which are the mean values of the data points shown in Figure 6. The standard deviations of $\Delta V_{\rm H\,I}$ and $T_{\rm bg}$ are $1.9\,{\rm km\,s^{-1}}$ and 0.05 K, respectively. Note that $\tau_{\rm H\,I} = 0.21$ is given in Appendix A. According to these curves, there is a trend that larger $\tau_{\rm H\,I}$ gives a smaller slope, which is consistent with the distribution of the low-$T_{\rm d}$ points. Therefore, these equal-$\tau_{\rm H\,I}$ curves should trace the distribution of the equal-$T_{\rm d}$ points. As shown in Figure 6, the curves to which $\alpha = 1.3$ is applied show better correlations with the distributions of the data points rather than $\alpha = 1.0$ for both high- and low-$T_{\rm d}$. This also suggests that it is important to take into account the dust evolution. We can say in addition that the small variances at high $T_{\rm d}$ (small $\tau_{\rm H\,I}$) suggest the uniform DGR and the uniform grain size.

Figure 7(a) is a spatial distribution of $N_{\rm H}$ calculated with Equation (3). Figure 7(b) shows a distribution of $N^*_{\rm H\,I}$ derived with Equation (4), which is the H I column number density at optically-thin limit. Note that in Figure 7(a) and (b) the scales of their color-bars are significantly different from each other. In Figure 7(c) we show a distribution of $N_{\rm H}/N^*_{\rm H\,I}$, which is the pixel-to-pixel ratio map of Figure 7(a) and (b). In this map,

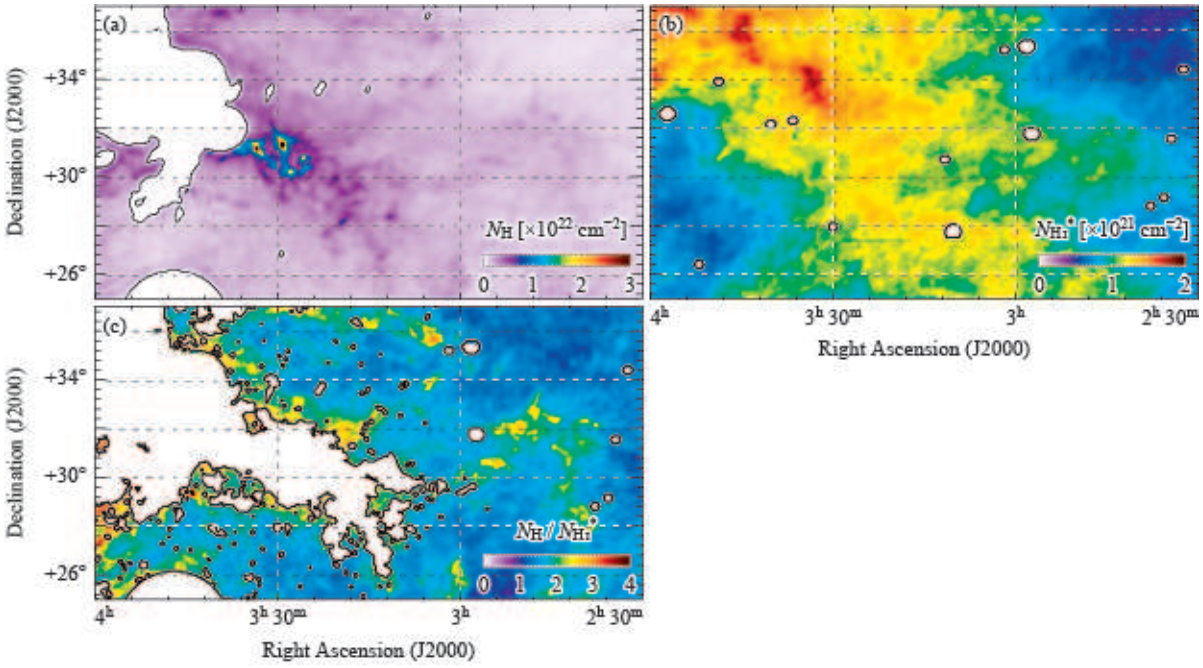

Figure 7. (a) A map of $N_{\rm H}$ calculated by Equation (3). Masks-(d), (e), (f) are applied. (b) A spatial distribution of H I column density calculated under the assumption of the optically thin limit, $N^*_{\rm HI}$ ($= X_{\rm HI} \times W_{\rm HI}$) Masks-(b), (c) are applied. (c) A pixel-to-pixel ratio map between (a) and (b) ($N_{\rm H}/N^*_{\rm HI}$). We found the mean value as $\langle N_{\rm H}/N^*_{\rm HI}\rangle \sim 1.8$. Mask-(a) is applied in addition.

mask-(a) is applied in order to exclude the data points where H_2 can exist. We found that the mean value of $N_{\rm H}/N^*_{\rm HI}$ is ∼1.8 (see also Figure 9), and hence in this region, the amount of H I is underestimated to be ∼57% if Equation (4) is used. From these, it turns out that H I optical depth has a significant effect in estimating the amount of H I gas in the ISM.

Using Equation (3), we can estimate the total (atomic and molecular) amount of the hydrogen gas in a high accuracy without being affected by H I optical depth. However, note that Equation (3) alone cannot separate atomic and molecular components, and also cannot separate individual components located along the same line of sight.

3.5. *$\tau_{H\,I}$ and T_s Estimation*

Once $N_{\rm H}$ is derived with Equation (3), $\tau_{\rm HI}$ and $T_{\rm s}$ can be calculated independently as solutions of a system of equations (5) and (6) (Fukui et al. 2014, 2015). Since the solutions of the coupled equations cannot be expressed analytically, they are numerically calculated. We note that in the limit of $\tau_{\rm HI} = 0$ the equations (5) and (6) become the same, therefore the solutions are indeterminate if the H I gas is assumed to be optically thin. Figure 8 shows the spatial distributions of (a) $\tau_{\rm HI}$ and (b) $T_{\rm s}$, respectively. In order to compare with the result of $\tau_{\rm HI}$ obtained based on H I absorption measurements in Stanimirović et al. (2014), we spatially interpolated (bilinear method) the H I spectra masked by mask-(c) and calculated the solutions.

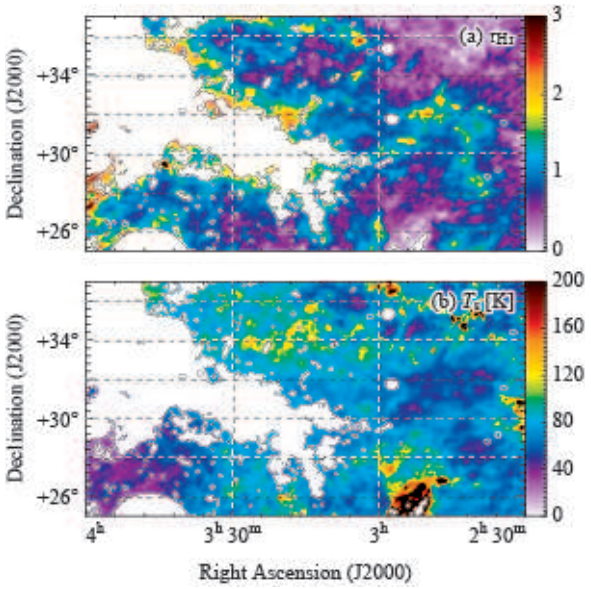

Figure 8. Estimated spatial distributions of (a) $\tau_{\rm HI}$ and (b) $T_{\rm s}$, which are the solutions of the system of equations (5) and (6). For the purpose of comparisons with the results of Stanimirović et al. (2014), we spatially interpolated the H I spectra toward the background sources using the bilinear interpolation method and computed $\tau_{\rm HI}$ and $T_{\rm s}$.

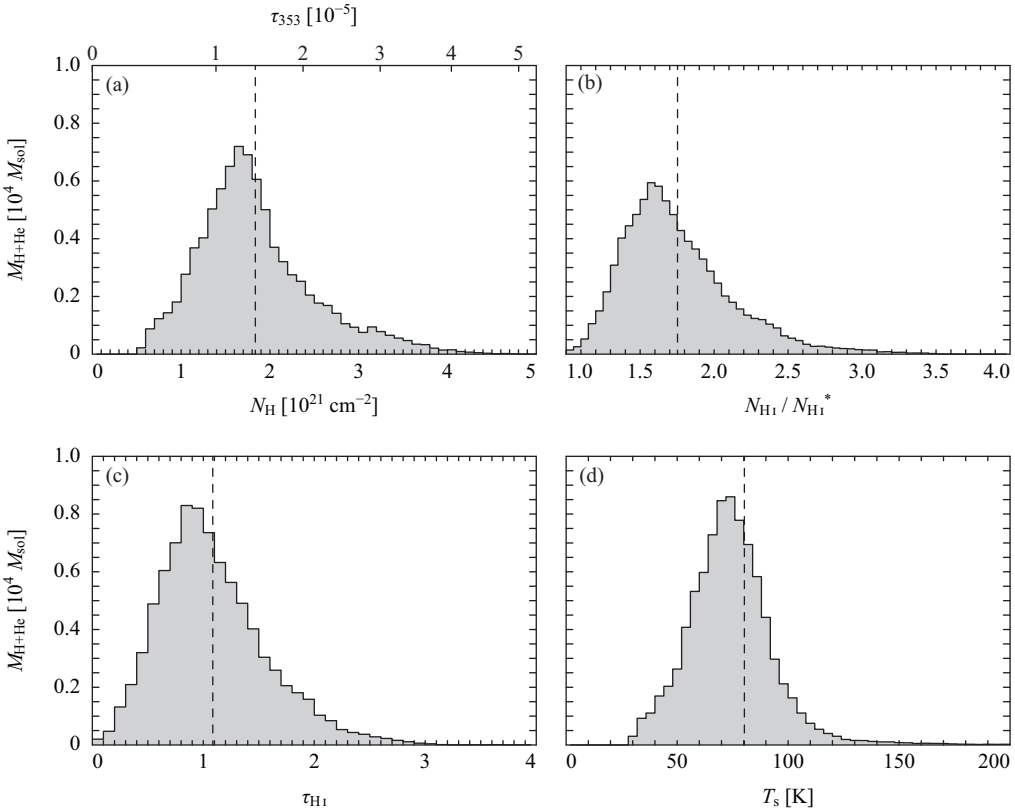

Figure 9. Mass-weighted histograms of (a) $N_{\rm H}$, (b) $N_{\rm HI}/N^*_{\rm HI}$, (c) $\tau_{\rm HI}$, and (d) $T_{\rm s}$ for the region shown in Figure (8). We assume a distance of 300 pc and the mass includes helium. The dashed lines indicate the mass-weighted mean values of each histogram. In panel (a) the upper x-axis shows the τ_{353} calculated by using Equation (3).

In Figure 9 we show mass-weighted histograms of (a) $N_{\rm H}$, (b) $N_{\rm H}/N^*_{\rm HI}$, (c) $\tau_{\rm HI}$, and (d) $T_{\rm s}$, respectively, for the region shown in Figure 8. We assumed the distance to the Perseus cloud as 300 pc (Bally et al. 2008), and the mass is calculated by including hydrogen and helium. We found the mass-weighted mean values as $\langle N_{\rm H}\rangle \sim 1.8\times10^{21}\,{\rm cm^{-2}}$, $\langle N_{\rm H}/N^*_{\rm HI}\rangle \sim 1.8$, $\langle\tau_{\rm HI}\rangle \sim 1.1$, and $\langle T_{\rm s}\rangle \sim 80\,{\rm K}$. The ratio of the H I mass with $\tau_{\rm HI}<1$ is ∼51% of the total mass and as shown in Figure 6 optically thick H I cannot be ignored. In Fukui et al. (2014) we found that $\langle T_{\rm s}\rangle \sim 30\,{\rm K}$ around the MBM 53, 54, 55/HLCG 92–35 clouds, which is somewhat lower than that for the Perseus region. It is possible that the Perseus cloud is located in the Gould's belt, which contains heat sources including some SFRs and OB associations.

Figure 10 shows examples of the $\tau_{\rm HI}$ and $T_{\rm s}$ solutions. The curves of Equation (5) (blue) and Equation (6) (red), and the solutions of $\tau_{\rm HI}$ and $T_{\rm s}$ (purple) are drawn on the $\tau_{\rm HI}$–$T_{\rm s}$ plane. We show the solutions toward the background radio sources described in Stanimirović et al. (2014). As described above, the H I spectra toward the directions are spatially interpolated. The blue and red dashed curves indicate $1\,\sigma$ uncertainties for each curve, and we defined the uncertainties in the solutions (purple lines) as the intersections of the dashed curves. Table 2 is the results of the calculations. For each data point the solutions of $\tau_{\rm HI}$ and $T_{\rm s}$ are well determined.

3.6. *X_{CO} estimation*

The $X_{\rm CO}$ factor, which is an empirical conversion factor, has been used in order to estimate H_2 column number density ($N_{\rm H_2}$) from the velocity-integrated intensity of the CO line ($W_{\rm CO}$). Conventionally, $X_{\rm CO}\sim$ (1–2) $\times\,10^{20}\,{\rm cm^{-2}\,K^{-1}\,km^{-1}\,s}$ is assumed as an typical value for the Galaxy (e.g., Bolatto et al. 2013). Here, since $N_{\rm H}$ is obtained with a higher accuracy, we are able to determine $X_{\rm CO}$ by using the *Planck* data and $W_{\rm CO}$ data.

Figure 11 indicates correlation plots between $W_{\rm CO}$ (x–axis) and $N_{\rm H}$ (y–axis). Fitting the distribution of the data points and calculating the slope and the intercept, we can separate the atomic component and the molecular component from $N_{\rm H}$.

$$N_{\rm H} = N_{\rm HI} + 2\,N_{\rm H_2}$$
$$N_{\rm H_2} = X_{\rm CO}\times W_{\rm CO}$$

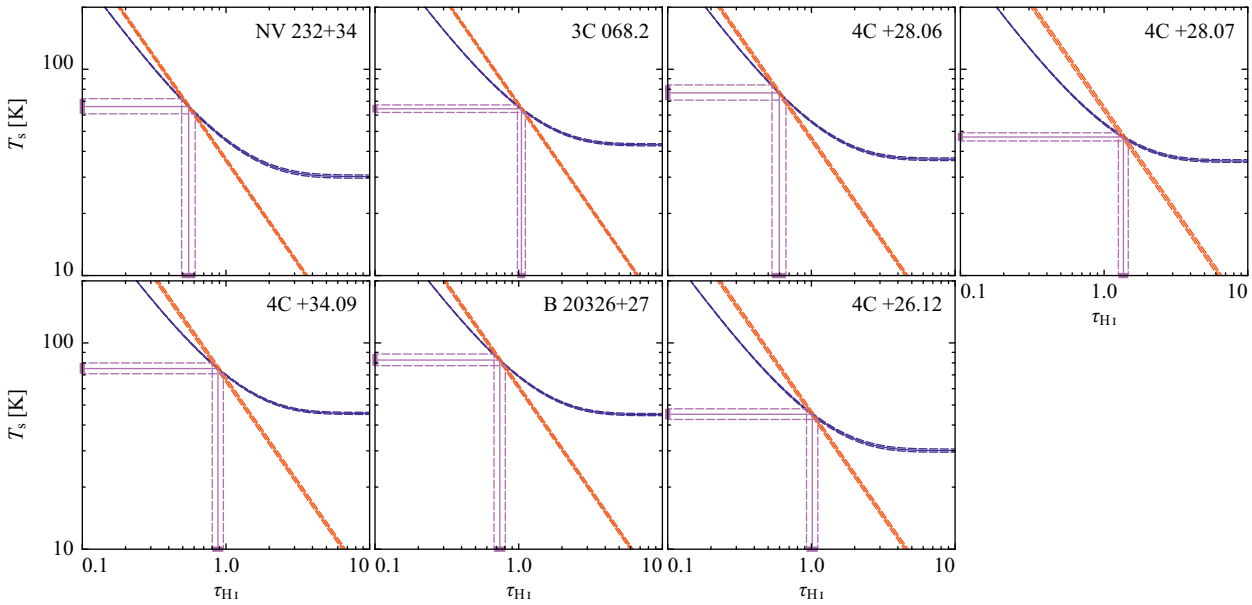

Figure 10. Examples of the $\tau_{\rm HI}$ and $T_{\rm s}$ estimations. As examples we show the results toward background radio sources described in Stanimirović et al. (2014). Blue solid lines are calculated by Equation (5) and red ones by Equation (6). The solutions of $\tau_{\rm HI}$ and $T_{\rm s}$ (purple solid lines) are obtained in terms of the intersections of the red and blue lines. Dashed lines indicate the uncertainty ranges for each solid line.

Table 2. List of radio continuum sources in Table 1 of Stanimirović et al. (2014)

				present study				Stanimirović et al. (2014)
Name	Position		τ_{353}	$N_{\rm H}$	$T_{\rm s}$	$\tau_{\rm HI}$	$\tau_{\rm HI} \times \Delta V_{\rm HI}$	$\int \tau_{\rm HI} dV$
	$\alpha_{\rm J2000}$	$\delta_{\rm J2000}$	[10^{-5}]	[10^{21} cm^{-2}]	[K]		[km s^{-1}]	[km s^{-1}]
(a)	(b)	(c)	(d)	(e)	(f)	(g)	(h)	(i)
NV 0232+34	$2^{\rm h}\,32^{\rm m}\,28\overset{\rm s}{.}72$	$+34^\circ\,24^{\rm m}\,06\overset{\rm s}{.}08$	0.5	0.8	66^{+6}_{-5}	0.5±0.1	6.8±0.7	1.89±0.14
3C 068.2	$2^{\rm h}\,34^{\rm m}\,23\overset{\rm s}{.}87$	$+31^\circ\,34^{\rm m}\,17\overset{\rm s}{.}62$	0.9	1.3	64^{+3}_{-3}	1.0±0.1	10.8±0.7	4.77±0.14
4C +28.06	$2^{\rm h}\,35^{\rm m}\,35\overset{\rm s}{.}41$	$+29^\circ\,08^{\rm m}\,57\overset{\rm s}{.}73$	0.7	1.1	77^{+7}_{-6}	0.6±0.1	7.7±0.9	3.67±0.04
4C +28.07	$2^{\rm h}\,37^{\rm m}\,52\overset{\rm s}{.}42$	$+28^\circ\,48^{\rm m}\,09\overset{\rm s}{.}16$	1.1	1.6	47^{+2}_{-2}	1.4±0.1	18.1±1.4	4.43±0.15
4C +34.09	$3^{\rm h}\,01^{\rm m}\,42\overset{\rm s}{.}38$	$+35^\circ\,12^{\rm m}\,20\overset{\rm s}{.}84$	1.1	1.5	75^{+5}_{-4}	0.9±0.1	11.0±1.0	4.05±0.04
4C +30.04	$3^{\rm h}\,11^{\rm m}\,35\overset{\rm s}{.}19$	$+30^\circ\,43^{\rm m}\,20\overset{\rm s}{.}62$	2.0	2.4	···	···	···	7.62±0.08
B 20326+27	$3^{\rm h}\,29^{\rm m}\,57\overset{\rm s}{.}69$	$+27^\circ\,56^{\rm m}\,15\overset{\rm s}{.}64$	1.2	1.6	83^{+6}_{-5}	0.7±0.1	10.3±0.9	4.50±0.04
3C 092	$3^{\rm h}\,40^{\rm m}\,08\overset{\rm s}{.}55$	$+32^\circ\,09^{\rm m}\,02\overset{\rm s}{.}32$	8.1	7.0	···	···	···	13.96±0.99
3C 093.1	$3^{\rm h}\,48^{\rm m}\,46\overset{\rm s}{.}93$	$+33^\circ\,53^{\rm m}\,15\overset{\rm s}{.}41$	2.2	2.6	···	···	···	8.93±0.23
4C +26.12	$3^{\rm h}\,52^{\rm m}\,04\overset{\rm s}{.}36$	$+26^\circ\,24^{\rm m}\,18\overset{\rm s}{.}11$	0.8	1.1	45^{+3}_{-3}	1.0±0.1	$13.9^{+1.3}_{-1.2}$	4.87±0.04

NOTE— (a), (b), and (c): Names and coordinates of the radio continuum sources listed in Table 1 of Stanimirović et al. (2014).
(d): τ_{353} values toward the sources.
(e): $N_{\rm H}$ values toward the sources calculated by Equation (3).
(f) and (g): H I spin temperature and H I optical depth calculated by Equations (5) and (6).
(h): Velocity-integrated H I optical depth derived from column (g) and $\Delta V_{\rm HI}$.
(i): Total Velocity-integrated H I optical depth derived from the Gaussian parameters of $\tau_{\rm HI}$ spectra of Stanimirović et al. (2014).

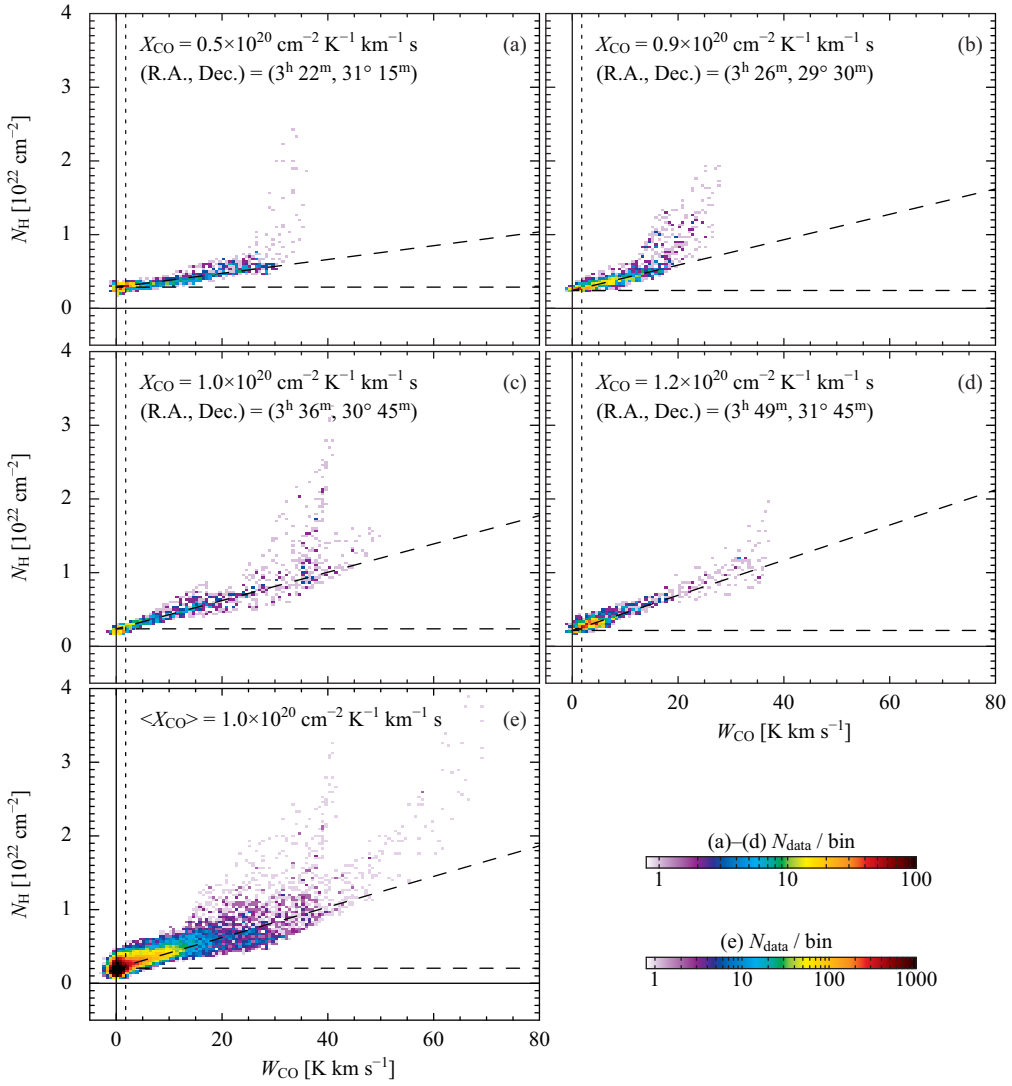

Figure 11. Examples of W_{CO}–N_H correlation plots (density plots) using the data points inside the $r = 1$ deg windows (A)–(D) shown in Figure 12. Outlier-robust linear regression method is used to fit data in order to avoid effects due to saturated points. The data points of $W_{CO} > 3\,\sigma$ are used. The dotted lines indicate $W_{CO} = 3\,\sigma$. The dashed lines show the resulting slopes and intercepts of the regressions, and X_{CO} is estimated by Equation (8) using these slopes.

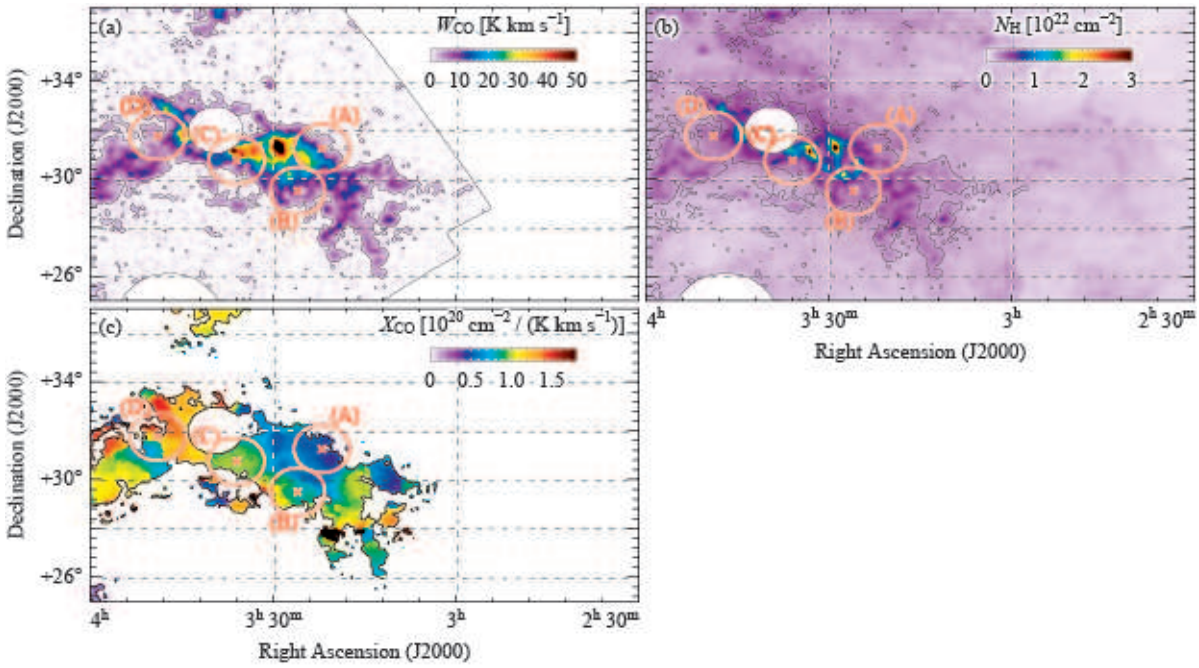

Figure 12. (a) The map of $W_{\rm CO}$ overlaid with $r = 1^\circ$ windows (A)–(D). (b) The map of $N_{\rm H}$ overlaid with the windows (A)–(D). (c) A map of the estimated spatial distribution of $X_{\rm CO}$ factor. The mean value of $X_{\rm CO}$ is $\langle X_{\rm CO}\rangle = 9.5 \times 10^{19}\,{\rm cm^{-2}\,K^{-1}\,km^{-1}\,s}$. In Figure (11) we show examples of $W_{\rm CO}$-$N_{\rm H}$ correlation plots using the data points inside the windows (A)–(D) used to compute $X_{\rm CO}$ at their center positions (X-points).

So, we obtain the following,

$$\begin{aligned} N_{\rm H} \quad &= (2\,X_{\rm CO})\,W_{\rm CO} + N_{\rm H\,I} \\ &\equiv ({\rm slope}) \times W_{\rm CO} + ({\rm intercept}). \end{aligned} \tag{8}$$

The intercept gives the atomic component, and the slope gives the molecular component and the $X_{\rm CO}$ factor (= slope/2). Note that the contribution of the atomic component is a mean value, and we assumed that it is constant against $W_{\rm CO}$. We used an outlier-robust linear regression method in order to avoid the effect due to the data points where $W_{\rm CO}$ is saturated against $N_{\rm H}$. For this purpose, we utilized the ROBUST_LINEFIT routine provided in The IDL Astronomy User's Library (Landsman 1993). In the present study, we estimated the spatial distribution of the $X_{\rm CO}$ factor by the procedure described below.

1. We prepare a "window", which extracts the data points within a 1-degree radius from a certain point. This radius is determined in order to ensure a sufficient number of data points to be fitted.

2. By using the data points inside the window, we estimate the $X_{\rm CO}$ factor from the $W_{\rm CO}$–$N_{\rm H}$ plot .

3. We regard the resulting $X_{\rm CO}$ as the value of the center point of the window.

4. The $X_{\rm CO}$ map can be obtained by iteratively calculating the $X_{\rm CO}$ factor for all the data points while moving the center of the window pixel by pixel (this process is similar to image convolution).

Figure 12(a) and (b) shows the map of $W_{\rm CO}$ and $N_{\rm H}$ (already shown in Figure 1(a) and Figure 7(a)), but only Mask-(d) and (e) are applied in order to compare with previous studies (Lee et al. 2012, 2014, described below). The four overlaid circles (A)–(D) indicate the examples of the "window", corresponding to the panels (a)–(d) of Figure 11, respectively. The resulting $X_{\rm CO}$ map is shown in Figure 12(c). We found the average value of this map is $\langle X_{\rm CO}\rangle \sim 9.5 \times 10^{19}\,{\rm cm^{-2}\,K^{-1}\,km^{-1}\,s}$, which is consistent with the empirical and typical value of the Galaxy, (1–2) $\times\, 10^{20}\,{\rm cm^{-2}\,K^{-1}\,km^{-1}\,s}$. On the other hand, Lee et al. (2012, 2014) also estimated a spatial distribution the $X_{\rm CO}$ factor in the Perseus molecular cloud. However, they obtained the average value of $\langle X_{\rm CO}\rangle \sim 0.3 \times 10^{20}\,{\rm cm^{-2}\,K^{-1}\,km^{-1}\,s}$, which is ∼1/3 of our result. We will explain this discrepancy between these two results on the $X_{\rm CO}$ factor in the next section.

4. DISCUSSIONS

4.1. X_{CO}

As mentioned above, Lee et al. (2012, 2014) also estimated the spatial distribution of the $X_{\rm CO}$ factor in the Perseus molecular cloud. Their procedure for the $X_{\rm CO}$ estimation is briefly described below:

1. $N_{\rm H}$ is estimated by using A_V as a tracer of the total amount of hydrogen. They used the dust-to-gas ratio (DGR) as the conversion factor,

$$N_{\rm H} = \frac{A_V}{\rm DGR}, \qquad {\rm DGR} = 1.1 \times 10^{-21}\,{\rm mag}^{-1}\,{\rm cm}^2.$$

2. $N_{\rm H_2}$ is calculated by subtracting $N_{\rm H\,I}$ from $N_{\rm H}$,

$$N_{\rm H_2} = \frac{1}{2}(N_{\rm H} - N_{\rm H\,I}). \qquad (9)$$

Note that in Lee et al. (2012, 2014) $\tau_{\rm H\,I} = 0$ is assumed, that is, $N_{\rm H\,I} = N^*_{\rm H\,I}$ is assumed.

3. The resulting $X_{\rm CO}$ map is obtained by dividing $N_{\rm H_2}$ by $W_{\rm CO}$ for each data point.

The available A_V map ("COMPLETE survey" (Lombardi & Alves 2001) based on the 2MASS data), however, covers only the central region of the cloud, hence they made a wide-area "simulated" A_V map by using *IRAS* data:

1. The wide-area dust temperature map was estimated from the ratio of the intensities of the IRIS $60, 100\,\mu$m maps. Effect from Very Small Grains (VSGs) was considered for the IRIS $60\,\mu$m map.

2. The wide-area map of optical depth at $100\,\mu$m (τ_{100}) was derived from the ratio of the IRIS $100\,\mu$m map to the intensity at $100\,\mu$m of the blackbody radiation at derived dust temperature. The zero point offset in τ_{100} was also corrected.

3. The wide-area "simulated" A_V map was obtained from the τ_{100} map by using the conversion factor obtained by the correlation between τ_{100} and the COMPLETE A_V map.

Figure 13(a) shows histograms of $X_{\rm CO}$ derived in Section 3.6 and $X_{\rm CO}$ reproduced by the same procedure as Lee et al. (2012, 2014). Note that the data points used are the same as Figure 12, not same as Lee et al. (2012, 2014). The average values are $\langle X_{\rm CO}\rangle \sim 9.5 \times 10^{19}\,{\rm cm^{-2}\,K^{-1}\,km^{-1}\,s}$ and $\langle X_{\rm CO}\rangle_{\rm Lee} \sim 4.0 \times 10^{19}\,{\rm cm^{-2}\,K^{-1}\,km^{-1}\,s}$ for the present study and the Lee's result, respectively, and the result of Lee et al. (2012, 2014) is well reproduced. In Figure 13(b) we show histograms of $N_{\rm H}$ derived by using Equation (3) and the same method as Lee et al. (2012). We found $\langle N_{\rm H}\rangle \sim 4.3 \times 10^{21}\,{\rm cm^{-2}}$ and $\langle N_{\rm H}\rangle_{\rm Lee} \sim 1.4 \times 10^{21}\,{\rm cm^{-2}}$, hence Lee et al. (2012) underestimated $N_{\rm H}$ to be ∼40%.

Here, we will quantitatively examine the difference in $X_{\rm CO}$ between the present study and Lee et al. (2012, 2014). Since $X_{\rm CO} = N_{\rm H_2}/W_{\rm CO}$, the underestimation of $X_{\rm CO}$ in Lee et al. (2012, 2014) is caused by the underestimation of $N_{\rm H_2}$ in Equation (9). Therefore, we investigated the cause of the underestimation of $N_{\rm H}$ and $N_{\rm H\,I}$ in Equation (9). Figure 14(a) is a correlation plot between τ_{353} and I_{100}. The correlation coefficient is ∼0.5 and we found that I_{100} is not a good tracer of $N_{\rm H}$. Figure 14(b) shows a correlation between $N_{\rm H}$ calculated by Equation (3) and $N_{\rm H}$ calculated by the same method as Lee et al. (2012). The dashed line indicates the 1:1 relationship. The latter is clearly underestimated (∼35% on average) against the former. Separately from that, in Lee et al. (2012, 2014) the effect of H I optical depth was not considered. As shown in Section 3.4 the effect of $\tau_{\rm H\,I}$ is $N_{\rm H\,I}/N^*_{\rm H\,I} \sim 1.8$. Therefore, $N_{\rm H\,I}$ is underestimated to be (at least) ∼57% on average. In addition, the integrated velocity range of H I spectra is from $-5\,{\rm km\,s^{-1}}$ to $+15\,{\rm km\,s^{-1}}$ in Lee et al. (2012). This corresponds to ∼76% of the total integrated intensity of the mean spectrum shown in Figure 3(b). From these, $N_{\rm H\,I}$ in Equation (9) is underestimated at least 57% × 76% ∼ 40% on average. In Lee et al. (2012, 2014), the right-hand side of Equation (9) is underestimated to be ∼40%, and hence, $X_{\rm CO}$ is underestimated to be ∼40% against our result.

4.2. *Mass*

The total mass of the hydrogen gas including H I, H_2, and helium is derived as $M_{\rm H} = 1.8 \times 10^5\,M_\odot$ by using $N_{\rm H}$ calculated by Equation (3). We assumed the distance to the Perseus cloud as 300 pc (Bally et al. 2008). On the other hand, the mass of the molecular hydrogen gas is calculated as $M_{\rm H_2} = 2.5 \times 10^4\,M_\odot$ by using $W_{\rm CO}$ and the $X_{\rm CO}$ map obtained in Section 3.6. From these masses, we calculate the mass of the atomic hydrogen gas as $M_{\rm H\,I} = M_{\rm H} - M_{\rm H_2} = 1.5 \times 10^5\,M_\odot$. This indicates that the molecular cloud is surrounded by the atomic gas whose mass is by an order of magnitude larger than that of the molecular one, and it also indicates that the atomic gas is the most principal component of the ISM. This is consistent with the result for the MBM 53, 54, 55/HLCG 92–35 region described in Fukui et al. (2014).

4.3. $\tau_{H\,I}$

As one of the previous studies on the atomic gas in the Perseus region, Stanimirović et al. (2014) calculated the H I optical depth toward 26 extra-Galactic radio continuum sources (such as quasars). They calculated $\tau_{\rm H\,I}$ as a function of velocity toward each radio source by using the method described in Heiles & Troland (2003). The calculated $\tau_{\rm H\,I}$ spectra were fitted with a sum of Gaussian functions, and the peak $\tau_{\rm H\,I}$ values and the Gaussian FWHMs (full width at half maximum) of each

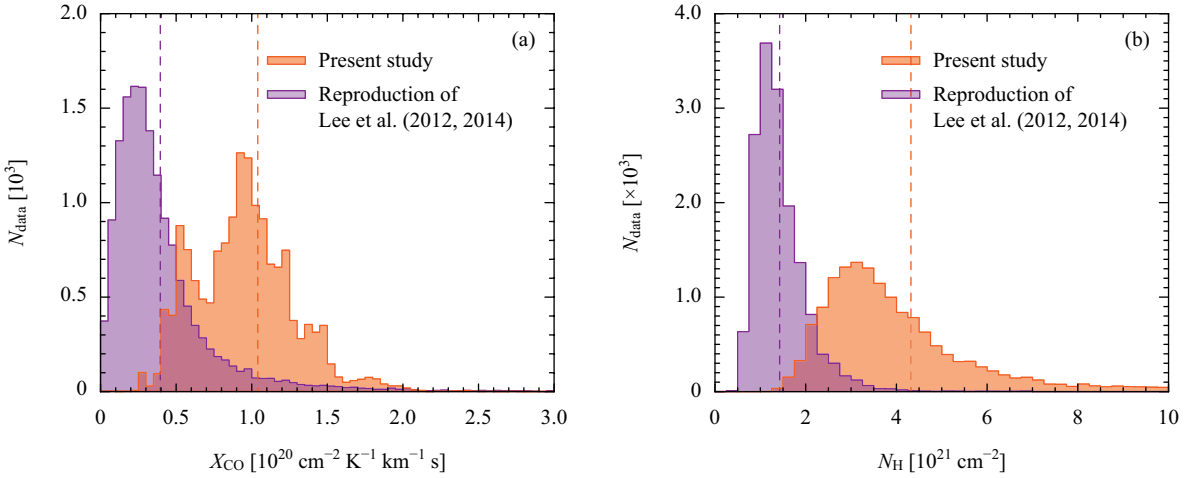

Figure 13. Histograms of (a) $X_{\rm CO}$ and (b) $N_{\rm H}$ for the region shown in Figure (12). The orange ones are obtaind in the present study and purple ones are obtained by replicating the procedures described in Lee et al. (2012, 2014). The dashed lines denote the mean values of each histogram.

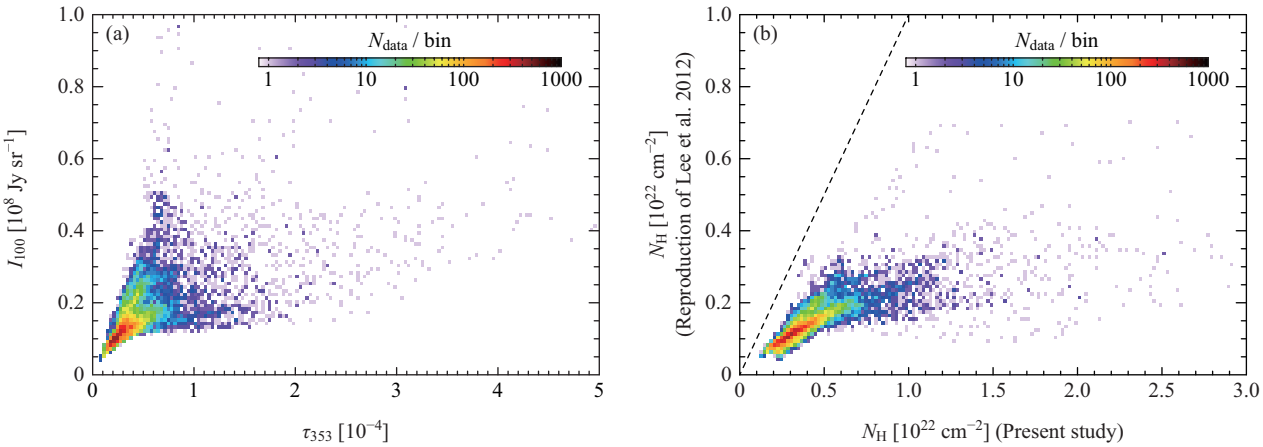

Figure 14. Correlation plots (density plots) between (a) τ_{353} and I_{100}, (b) $N_{\rm H}$ calculated by Equation (3) and $N_{\rm H}$ calculated by the same method as Lee et al. (2012). The dashed line in panel (b) indicates the 1:1 relationship.

velocity component were derived. However, they found the optically-thick H I gas only toward ∼15% of lines of sight. We test the results in Stanimirović et al. (2014) and Fukui et al. (2014, 2015), which differ a factor of several. To do this, we compare $\tau_{\rm H\,I}$ derived in Stanimirović et al. (2014) and that obtained in Section 3.5. Since our $\tau_{\rm H\,I}$ corresponds to the average value within given velocity width ($\Delta V_{\rm H\,I}$) (see Section 3.4) we compare the following two values toward each radio source located in the region we analyzed; (1) the sum of the areas of each Gaussian component of the $\tau_{\rm H\,I}$ profiles calculated in Stanimirović et al. (2014), and (2) the products of our $\tau_{\rm H\,I}$ and $\Delta V_{\rm H\,I}$. The results are listed in the column 8 and 9 of Table 2. Note that 4C +30.04, 3C 092, and 3C 093.1 are located at the masked area, therefore $\tau_{\rm H\,I}$ cannot be calculated by our method toward them. Although there is a rough positive correlation between them, they differ 2–4 times as a concrete numerical value. The correlation between them is plotted in Figure 15. The solid line indicates the one-to-one relationship (slope = 1), and the dashed line is the best-fit regression line through the origin (slope = 2.6). The results in Stanimirović et al. (2014) are systematically smaller than our results, and it is obvious that there is a discrepancy between these two results. This discrepancy can, however, be explained by characteristics of the data used to derive $\tau_{\rm H\,I}$ in the present study and Stanimirović et al. (2014).

In Stanimirović et al. (2014) $\tau_{\rm H\,I}$ is calculated based on the 21 cm absorption spectrum toward the extra-Galactic point sources. Since these point sources have infinitesimal apparent size, the absorption by the H I gas actually occurs toward the very direction of each source. However, Inoue & Inutsuka (2012) and McClure-Griffiths et al. (2006) revealed that the cold neutral

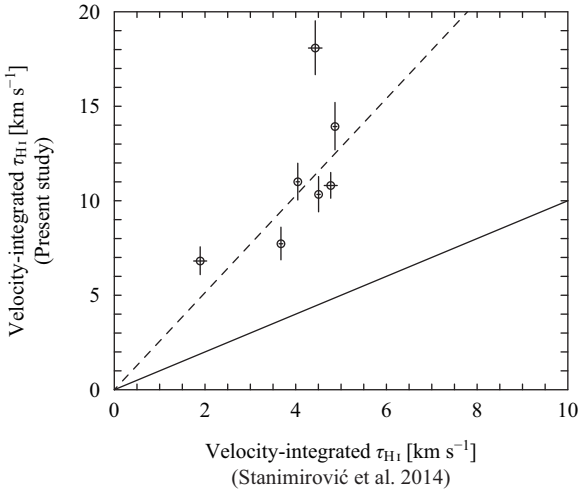

Figure 15. A correlation plot between velocity-integrated values of $\tau_{\rm HI}$ derived in Stanimirović et al. (2014) (x-axis) and $\tau_{\rm HI} \times \Delta V_{\rm HI}$ derived in the present study (y-axis). The solid line indicates the 1:1 relationship between both variables. The dashed line is the result of a linear regression through the origin. Its slope is 2.6.

medium (CNM), which is an optically-thick component of the HI gas, has highly filamentary and spatially inhomogeneous structure. Based on the three-dimensional numerical simulation of magnetohydrodynamics (MHD) (Inoue & Inutsuka 2012), we found that the CNM accounts for typically $\lesssim$20% of the 2D-projected area. Hence, the probability with which the CNM affects the absorption toward the point sources is small. Therefore, unless the observational beam size is not infinitesimal, absorption measurements tend to detect only warm neutral medium (WNM) and tend to regard the optical depth of the WNM as the average value within the beam. On the other hand, we use the emission data of gas and dust, and they include information from both the CNM and the WNM within the large beam ($\gtrsim$4 arcmin). Hence, we can say that the discrepancy of $\tau_{\rm HI}$ is due to the difference between the measurement methods (absorption toward point sources or emission). We present a full account on this effect by using the numerical simulation separately in Fukui et al. (2017).

5. CONCLUSIONS

In the present paper, we discussed the amount of the interstellar hydrogen gas and HI optical depth in the Perseus region by using the dust emission parameters obtained *Planck*, HI 21 cm line, and CO line data. The results are as follows:

1. The distributions of the data points on the τ_{353}–$W_{\rm HI}$ plot systematically vary by the change in $T_{\rm d}$. This is consistent with the results in Fukui et al. (2014, 2015), which is that HI optical depth cannot be ignored for the low-$T_{\rm d}$ points. However, since the distance to the Perseus region is larger than that to the region analyzed in Fukui et al. (2014, 2015) and there exist the SFRs, the τ_{353}–$W_{\rm HI}$ plot is somewhat complicated as compared with the local clouds.

2. In order to consider the dust evolution at high density regions, we calibrated the τ_{353}–$N_{\rm H}$ relationship by using the extinction at J-band. As with Roy et al. (2013), we confirmed that τ_{353} becomes larger as a function of the 1.3-th power of $N_{\rm H}$ ($\alpha = 1.3$). In addition, we reconsidered the reference values of τ_{353} and $N_{\rm H}$ in Equation (2) by referring to the results in Fukui et al. (2014). The calibrated τ_{353}–$N_{\rm H}$ relationship (Equation (3)) yields $\sim$20% smaller $N_{\rm H}$ than that in the case of $\alpha = 1.0$. By using this relationship we can calculate $N_{\rm H}$ from τ_{353} more accurately, taking the dust evolution into account.

3. Compared with the present method, the conventional method which assumes that the HI gas is optically-thin, underestimates the amount of the hydrogen gas to be $\sim$57% in the Perseus region. Optical depth of the HI gas ($\tau_{\rm HI}$) and spin temperature ($T_{\rm s}$) can be calculated, and we obtain $\langle \tau_{\rm HI} \rangle \sim 1.1$. These results support that there exists a large amount of optically-thick HI gas around the molecular clouds. The arguments by Fukui et al. (2014, 2015) still hold in the region where the density is relatively high and there exist the SFRs.

4. By using $N_{\rm H}$ calculated from τ_{353} and the CO intensity ($W_{\rm CO}$), we estimated the spatial distribution of $X_{\rm CO}$. We obtained $\langle X_{\rm CO} \rangle \sim 9.5 \times 10^{19}\,{\rm cm^{-2}\,K^{-1}\,km^{-1}\,s}$, which is consistent with the conventional value in the Galaxy, $X_{\rm CO} \sim$ (1–2) $\times\, 10^{20}\,{\rm cm^{-2}\,K^{-1}\,km^{-1}\,s}$. Although the result in Lee et al. (2012, 2014) is underestimated to be $\sim$40% compared to this result, this discrepancy in the $X_{\rm CO}$ maps can be quantitatively explained by the difference of the data used in order to calculate $N_{\rm H}$, the effect of the optical depth of HI, and the difference of the integrated velocity ranges of HI 21 cm spectra.

5. We compared our $\tau_{\rm HI}$ with that obtained in Stanimirović et al. (2014). When the optical depth is calculated based on the absorption measurements toward the background point sources, it can be

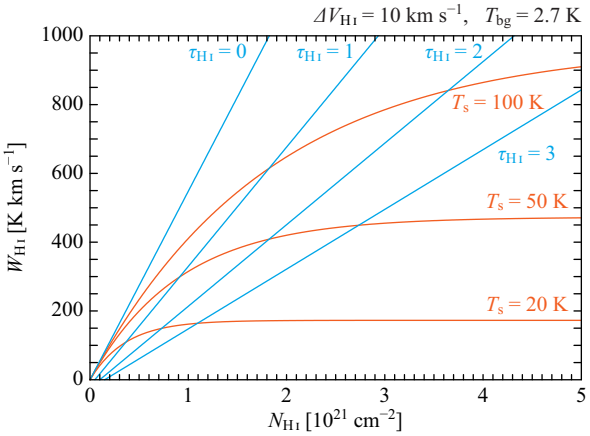

Figure 16. Theoretical curves of $W_{\rm H\,I}$ as functions of $N_{\rm H\,I}$. The light-blue ones are for the case of fixing $\tau_{\rm H\,I} = 0, 1, 2, 3$, and the orange ones $T_{\rm s} = 20, 50, 100\,{\rm K}$. $\Delta V_{\rm H\,I} = 10\,{\rm km\,s^{-1}}$ and $T_{\rm bg} = 2.7\,{\rm K}$ are assumed.

underestimated to be ∼40% on the average compared to that obtained based on the gas/dust emission data. It is revealed that the cold H I gas (CNM) has highly filamentary distribution by numerical simulation studies (e.g., Inoue & Inutsuka 2012). Therefore, the probability with which the optically-thick H I filaments lie on the infinitesimal apparent-size sources is small, ∼20%. The underestimation of $\tau_{\rm H\,I}$ in absorption measurements is consistent with this picture.

This work was financially supported by Grants-in-Aid for Scientific Research (KAKENHI) of the Japan society for the Promotion of Science (JSPS) Grant Numbers 15H05694, 25287035.

This research has made use of NASA's Astrophysics Data System.This publication utilizes data from Galactic ALFA H I (GALFA H I) survey data set obtained with the Arecibo L-band Feed Array (ALFA) on the Arecibo 305m telescope. Arecibo Observatory is part of the National Astronomy and Ionosphere Center, which is operated by Cornell University under Cooperative Agreement with the U.S. National Science Foundation. The GALFA H I surveys are funded by the NSF through grants to Columbia University, the University of Wisconsin, and the University of California.Based on observations obtained with *Planck* (`http://www.esa.int/Planck`), an ESA science mission with instruments and contributions directly funded by ESA Member States, NASA, and Canada.We acknowledge the use of the Legacy Archive for Microwave Background Data Analysis (LAMBDA), part of the High Energy Astrophysics Science Archive Center (HEASARC). HEASARC/LAMBDA is a service of the Astrophysics Science Division at the NASA Goddard Space Flight Center.This research has made use of the NASA/IPAC Infrared Science Archive, which is operated by the Jet Propulsion Laboratory, California Institute of Technology, under contract with the National Aeronautics and Space Administration.The CO line data was obtained with the CfA (Harvard-Smithsonian Center for Astrophysics) 1.2 m telescope (Dame et al. 2001). The Hα emission data was assembled from the Wisconsin H-Alpha Mapper (WHAM), the Virginia Tech Spectral-Line Survey (VTSS), and the Southern H-Alpha Sky Survey Atlas (SHASSA) (Finkbeiner 2003). Some of the results in this paper have been derived using the HEALPix (Górski et al. 2005) package.

APPENDIX

A. DETERMINATION OF $\tau_{353,\rm ref}$ AND $N_{\rm H,ref}$

$\tau_{353,\rm ref}$ and $N_{\rm H,ref}$ are the normalization constants conveniently introduced in order to nondimensionalize the both sides of Equation (2). Although in Fukui et al. (2015) $\tau_{353,\rm ref}$ and $N_{\rm H,ref}$ are determined as 4.77×10^{-6} and 1×10^{21} cm^{-2}, respectively, we derive our $\tau_{353,\rm ref}$ and $N_{\rm H,ref}$ for the Perseus region by using Equation (7). By giving α, $\tau_{\rm H\,I}$, and using $N_{\rm H,ref} = (1.15\times10^{8})\times X_{\rm H\,I}\times\tau_{353,\rm ref}$ (Fukui et al. 2015) we make the free parameter in Equation (7) $\tau_{353,\rm ref}$ alone, and determine it from the τ_{353}-$W_{\rm H\,I}$ plot. First, we describe the estimation of $\tau_{\rm H\,I}$ for high-$T_{\rm d}$ points in the Perseus region.

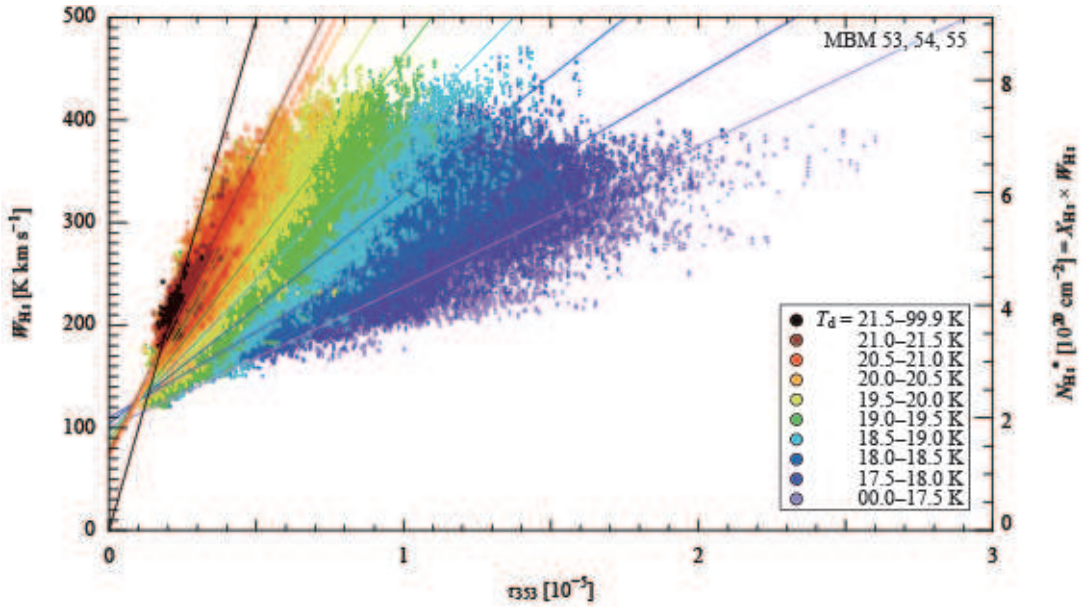

Figure 17. A τ_{353}-$W_{\rm H\,I}$ correlation plot in the MBM 53, 54, 55/HLCG 92–35 region colored by $T_{\rm d}$. We used the *Planck* dust data R1.20 unlike Fukui et al. (2014). The results of RMA (reduced major axis) regressions for each $T_{\rm d}$ range are also plotted. We assumed that H I gas is completely optically-thin for the data points of $T_{\rm d} \geq 21.5$ K (Fukui et al. 2014), therefore we make the regression line for $T_{\rm d} \geq 21.5$ K pass through the origin.

Figure 16 shows theoretical relationships between $N_{\rm H\,I}$ and $W_{\rm H\,I}$ in the cases of fixing $\tau_{\rm H\,I} = 0, 1, 2, 3$ or $T_{\rm s} = 20, 50, 100$ K. We assumed that $\Delta V_{\rm H\,I} = 10\,{\rm km\,s^{-1}}$ and $T_{\rm bg} = 2.7$ K. One can see that the variation width in $W_{\rm H\,I}$ becomes larger when $\tau_{\rm H\,I}$ becomes higher even if $T_{\rm s}$ is a constant (orange curves).

Figure 17 is the τ_{353}-$W_{\rm H\,I}$ correlation plot in the MBM 53, 54, 55 region colored by $T_{\rm d}$ in windows of 0.5 K intervals (Fukui et al. 2014) (similar to Figure 6 in the present paper). Masks are applied in order to exclude the data points where CO line is detected or radio point sources are located nearby, etc. (Fukui et al. 2014). Note that we used the *Planck* dust data R1.20 unlike Fukui et al. (2014). If we regard τ_{353} as a tracer of $N_{\rm H}$ and if there is a positive correlation relationship between $T_{\rm d}$ and $T_{\rm s}$, Figure 16 and 17 can roughly be considered as the same thing. Since it is thought that $\tau_{\rm H\,I}$ is larger if $T_{\rm d}$ is lower, the variation width in $W_{\rm H\,I}$ for the low-$T_{\rm d}$ points is relatively large in Figure 17, and vice versa. Accordingly, we performed linear fittings for each $T_{\rm d}$ range and examined variances from each regression line. We used the reduced major axis (RMA) regression method (e.g., Isobe et al. 1990), which minimizes the sum of the areas of the right-angled triangles delimited by each data point and the regression line, $\sum S_i$, and we defined the variance as the mean of the areas of the triangles, $\langle S_i \rangle$.

The results are shown in Table 3 and in Figure 18. In the MBM 53, 54, 55 region, an anti-correlation relationship between $T_{\rm d}$ and $\langle S_i \rangle$ can obviously be seen (the columns 1 and 2 of Table 3, and Figure 18(a)). The column 3 of Table 3 shows the mean $\tau_{\rm H\,I}$ values for each $T_{\rm d}$ range derived by using the method described in Fukui et al. (2014), and we can see a positive correlation relationship against $\langle S_i \rangle$ (see also Figure 18(b)). Therefore, $\langle \tau_{\rm H\,I} \rangle$ for $T_{\rm d} \geq 20.0$ K for the Perseus region can be estimated by using the $\langle \tau_{\rm H\,I} \rangle$–$\langle S_i \rangle$ relationship for the MBM 53, 54, 55 region as a template. The solid line in Figure 18(b) indicates the result of a linear fitting for the $\langle \tau_{\rm H\,I} \rangle$–$\langle S_i \rangle$ relationship. By referring this line we get $\langle \tau_{\rm H\,I} \rangle$ for $T_{\rm d} \geq 20.0$ K for the Perseus region as $\langle \tau_{\rm H\,I} \rangle = 0.21$ from $\langle S_i \rangle = 0.5 \times 10^{-5}\,{\rm K\,km\,s^{-1}}$ (the dashed lines).

By applying this $\langle \tau_{\rm H\,I} \rangle$ into Equation (7) and with this function fitting the data points of $T_{\rm d} \geq 20.0$ K, $\tau_{353,{\rm ref}}$ for the Perseus region can be calculated. Note that $\alpha = 1.3$ was applied and we used the relationship of $N_{\rm H,ref} = (1.15 \times 10^8) \times X_{\rm H\,I} \times \tau_{353,{\rm ref}}$ (Fukui et al. 2015). The result of the fitting is plotted in Figure 19, and we get $\tau_{353,{\rm ref}} = 1.6 \times 10^{-6}$ and $N_{\rm H,ref} = 3.4 \times 10^{20}\,{\rm cm^{-2}}$. The right-hand and left-hand dashed curve show the result for the case of $\tau_{353,{\rm ref}} = 8.7 \times 10^{-7}$, and $\tau_{353,{\rm ref}} = 4.77 \times 10^{-6}$ (Fukui et al. 2015), respectively. Both of them cannot trace the distribution of the data points of $T_{\rm d} \geq 20.0$ K.

Table 3. Relationship between $T_{\rm d}$, $\langle S_i \rangle$, and $\langle \tau_{\rm HI} \rangle$

	MBM 53, 54, 55		Perseus
$T_{\rm d}$	$\langle S_i \rangle$	$\langle \tau_{\rm HI} \rangle$	$\langle S_i \rangle$
[K]	$[10^{-5}\,{\rm K\,km\,s^{-1}}]$		$[10^{-5}\,{\rm K\,km\,s^{-1}}]$
(a)	(b)	(c)	(d)
$21.5 \leq$	0.3	0.1	···
21.0–21.5	0.3	0.1	···
20.5–21.0	0.6	0.3	···
20.0–20.5	0.8	0.4	0.5
19.5–20.0	0.9	0.5	0.7
19.0–19.5	1.4	0.8	2.1
18.5–19.0	1.9	1.2	18.8
18.0–18.5	2.8	1.7	23.8
17.5–18.0	5.5	2.7	32.2
< 17.5	6.5	3.8	34.6

NOTE—The dispersions of the data points from the regression lines shown in Figure 17. (a) The $T_{\rm d}$ range. (b) and (c) The dispersions of the data points defined in the text, and the mean value of $\tau_{\rm HI}$ estimated in Fukui et al. (2014). We use the relationship between these two as a template. (d) The dispersions of the data points in the Perseus region.

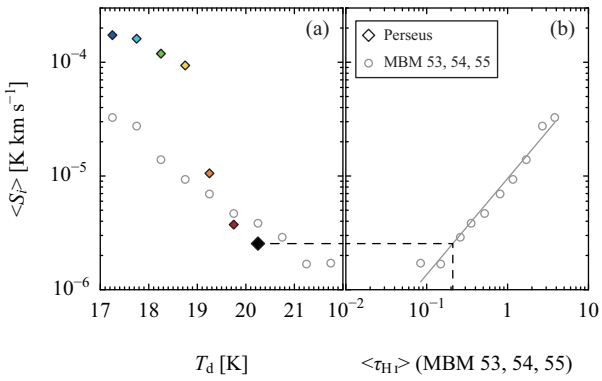

Figure 18. (a) Dispersions of the data points for each $T_{\rm d}$ range. The open circles indicate the results for the MBM 53, 54, 55 region and we use this as a template. The diamonds indicate the result for the Perseus region. The colors of the diamonds are the same as Figure 19. (b) The relationship between $\langle \tau_{\rm HI} \rangle$ (average of $\tau_{\rm HI}$ derived by the same method as Fukui et al. 2014) and the variance for each $T_{\rm d}$ range (MBM 53, 54, 55 template). The solid line indicates the result of a linear fit. The horizontal dashed line denotes $\langle S_i \rangle$ for the range of $T_{\rm d} > 20.0\,{\rm K}$, and the vertical dashed line the corresponding $\langle \tau_{\rm HI} \rangle$ ($= 0.21$).

From the above results, we adopted $\alpha = 1.3$, $\tau_{353,{\rm ref}} = 1.6 \times 10^{-6}$, and $N_{\rm H,ref} = 3.4 \times 10^{20}\,{\rm cm^{-2}}$ for the Perseus region.

REFERENCES

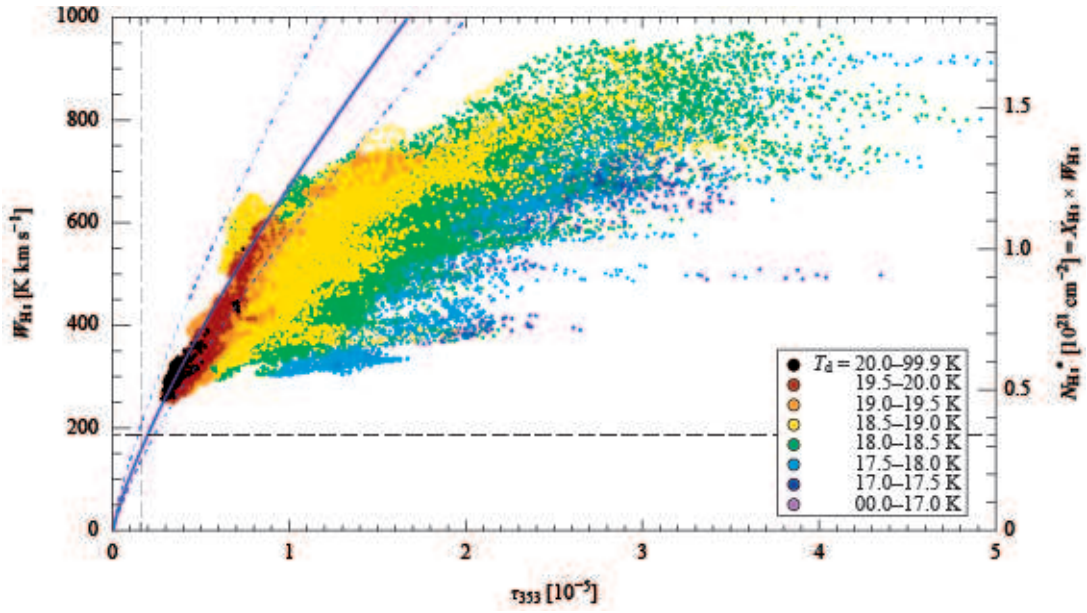

Figure 19. The τ_{353}-$W_{\rm H\,I}$ plot in the Perseus region. The right hand y-axis indicates the column number density of H I in the optically-thin limit ($N_{\rm H\,I}$). Fitting the data points which $T_{\rm d} > 20.0$ K with the theoretical function fixing $\alpha = 1.3$, and $\tau_{\rm H\,I} = 0.21$, we get $\tau_{353,\rm ref} = 1.6\times10^{-6}$. Note that we use the relationship described in Fukui et al. (2015), $N_{\rm H,ref} = (1.15\times10^{8})\times X_{\rm H\,I}\times\tau_{353,\rm ref}$. The right dotted line indicates the case which $\tau_{353,\rm ref} = 8.7 \times 10^{-7}$, and the left one the case which $\tau_{353,\rm ref} = 4.77 \times 10^{-6}$. The dashed lines correspond to $\tau_{353,\rm ref} = 1.6 \times 10^{-6}$ and $N_{\rm H,ref} = 3.4 \times 10^{20}$ cm^{-2}.

Bally, J., Walawender, J., Johnstone, D., Kirk, H., & Goodman, A. 2008, The Perseus Cloud, ed. B. Reipurth, 308

Bolatto, A. D., Wolfire, M., & Leroy, A. K. 2013, ARA&A, 51, 207

Dame, T. M., Hartmann, D., & Thaddeus, P. 2001, ApJ, 547, 792

Dickey, J. M., & Lockman, F. J. 1990, ARA&A, 28, 215

Draine, B. T. 2011, Physics of the Interstellar and Intergalactic Medium

Finkbeiner, D. P. 2003, ApJS, 146, 407

Forbrich, J., Lada, C. J., Lombardi, M., Román-Zúñiga, C., & Alves, J. 2015, A&A, 580, A114

Fukui, Y., Torii, K., Onishi, T., et al. 2015, ApJ, 798, 6

Fukui, Y., Okamoto, R., Kaji, R., et al. 2014, ApJ, 796, 59

Górski, K. M., Hivon, E., Banday, A. J., et al. 2005, ApJ, 622, 759

Heiles, C., & Troland, T. H. 2003, ApJS, 145, 329

Inoue, T., & Inutsuka, S.-i. 2012, ApJ, 759, 35

Isobe, T., Feigelson, E. D., Akritas, M. G., & Babu, G. J. 1990, ApJ, 364, 104

Jones, A. P., Fanciullo, L., Köhler, M., et al. 2013, A&A, 558, A62

Juvela, M., & Montillaud, J. 2016, A&A, 585, A38

Landsman, W. B. 1993, in Astronomical Society of the Pacific Conference Series, Vol. 52, Astronomical Data Analysis Software and Systems II, ed. R. J. Hanisch, R. J. V. Brissenden, & J. Barnes, 246

Lee, M.-Y., Stanimirović, S., Wolfire, M. G., et al. 2014, ApJ, 784, 80

Lee, M.-Y., Stanimirović, S., Douglas, K. A., et al. 2012, ApJ, 748, 75

Lombardi, M., & Alves, J. 2001, A&A, 377, 1023

McClure-Griffiths, N. M., Dickey, J. M., Gaensler, B. M., Green, A. J., & Haverkorn, M. 2006, ApJ, 652, 1339

Miville-Deschênes, M.-A., & Lagache, G. 2005, ApJS, 157, 302

Peek, J. E. G., Heiles, C., Douglas, K. A., et al. 2011, ApJS, 194, 20

Planck Collaboration, Ade, P. A. R., Aghanim, N., et al. 2011a, A&A, 536, A1

Planck Collaboration, Abergel, A., Ade, P. A. R., et al. 2011b, A&A, 536, A24

—. 2014, A&A, 571, A11

Reich, P., & Reich, W. 1986, A&AS, 63, 205

Reich, W. 1982, A&AS, 48, 219

Ridge, N. A., Schnee, S. L., Goodman, A. A., & Foster, J. B. 2006, ApJ, 643, 932

Roy, A., Martin, P. G., Polychroni, D., et al. 2013, ApJ, 763, 55

Sofue, Y. 2013, PASJ, 65, 118

Stanimirović, S., Murray, C. E., Lee, M.-Y., Heiles, C., & Miller, J. 2014, ApJ, 793, 132

Tóth, L. V., Marton, G., Zahorecz, S., et al. 2014, PASJ, 66, 17

Wenger, M., Ochsenbein, F., Egret, D., et al. 2000, A&AS, 143, 9

Ysard, N., Köhler, M., Jones, A., et al. 2015, A&A, 577, A110